ABSTRACT

Title of Document: ADVANCED SHADOW MOIRE WITH NON-CONVENTIONAL IMAGING ANGLES

Brian Kwong
Master of Science
Summer 2012

Directed By: Professor Bongtae Han,
Dept of Mechanical Engineering

With the increasingly smaller electronic package size, warpage of electronic packages becomes an important measurement related to the reliability of the products. Higher sensitivity out-of-plane deformation techniques are required to capture the smaller deformations of tiny packages for enhanced design analysis and model verification. The higher sensitivity is realized using non-zero viewing angles with the conventional shadow moiré technique. Advanced configurations to accommodate the non-zero viewing angles are developed to cope with direct reflection encountered on the conventional setup. An expanded governing equation for the configuration is derived and verified experimentally. Then the proposed configuration was implemented in the testing of an actual package to demonstrate the advantages that accrue from the higher sensitivity.

.

ADVANCED SHADOW MOIRE WITH NON-CONVENTIONAL IMAGING ANGLES

By

Brian John Kwong

Thesis submitted to the Faculty of the Graduate School of the
University of Maryland, College Park, in partial fulfillment
of the requirements for the degree of
Master of Science
2012

Advisory Committee:
Professor Bongtae Han (Chair)
Associate Professor Miao Yu
Associate Professor Patrick McCluskey

Acknowledgements

I want to express my gratitude and thanks to all the people whose help and support made this work possible. In particular, I want to specially thank Professor Han, my advisor for taking the time to educate me and allowing me to grow under his tutelage. Without his support and guidance I would not be the person I am today.

I also want to thank my friends in the lab for their collaboration throughout the past two years. This graduate school experience would have been a struggle if I wasn't in such an accepting group. Therefore it is my great pleasure to thank and acknowledge Bong-min, Dae-suk, Kenny, Michelle, Stephen, and Yong. To my friends and family outside the lab please accept my thanks for providing me the much needed anchor to the real world.

Finally, I want to thank my parents, Salina and Kelvin, for all their assistance and love. I am forever grateful and indebted for everything they have given me.

Table of Contents

List of Figures

Chapter 1: Motivation

Introduction to Warpage Measurement Techniques

The need for small displacement measurements came from the microelectronic industry as electronics and their packages trended smaller [1]. The electronic package is part of a final commercial device that has several functions including protection of components and interconnects, signal and power distribution, and mechanical support [2]. The whole device is comprised of multiple materials with individual coefficient of thermal expansion (CTE).

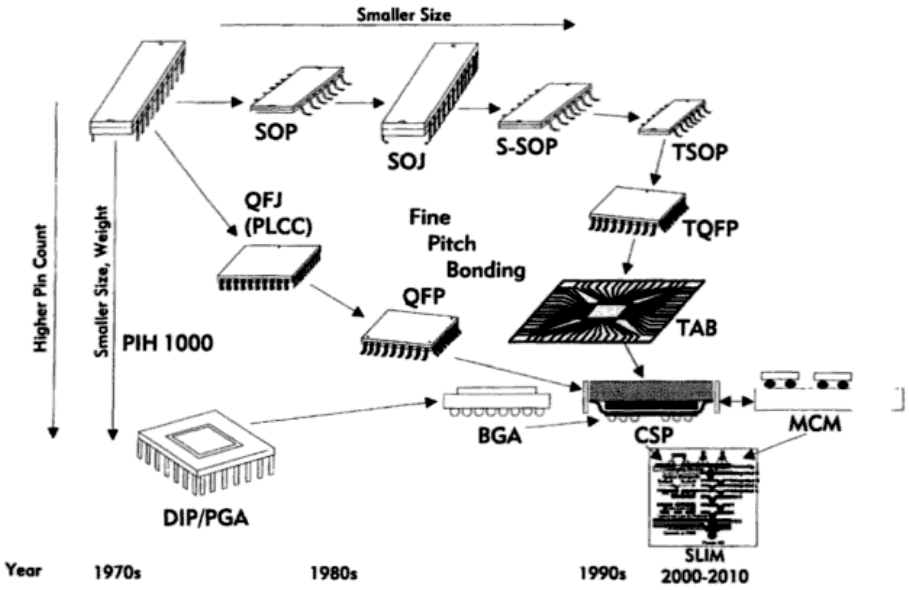

Figure 1.1: Example of package and industry trend [1]

Warpages in PBGA packages occur when materials with different CTE are mechanically bonded together and subject to a temperature change. The coefficient mismatch induces warpages as higher CTE material will have expanded more. At different temperatures other than the condition where the surfaces were initially flat, there will be more

deformation in one of the materials, leading to warpage. An example of the problem that arises during manufacturing is shown in Figure 1.2. Due to the CTE mismatch, the solder balls are no longer at the same height after undergoing thermal cycling. This causes reliability issues between interconnects due to the small differences in the height of the solder balls have the potential to affect solder ball fatigue life. Package warpage is associated with the reliability of the packaged device. Therefore, measurement of distortion in packages has been used in order to better model the changes to the package that occurs under extreme loads like thermal loads from the solder reflow process. Different techniques have been developed to cover the range of out of plane measurements.

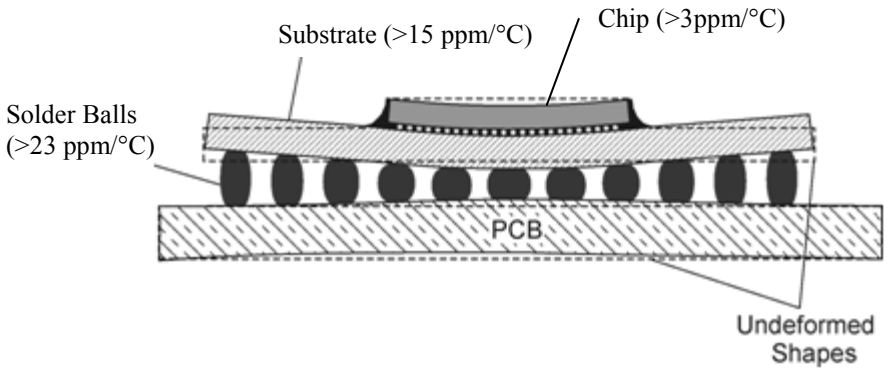

Figure 1.2 Cross-section of Ball Grid Array package with material CTE [3]

Shadow moiré, an out-of-plane displacement fringe pattern measurement technique, came about from the moiré topography concept first described by Takasaki [4] and Meadows et al. [5] in 1970. Shadow moiré has become a popular choice for sample distortion evaluation under mechanical and/or thermal loading in the microelectronics industry. A JEDEC industry standard for high temperature testing adopted shadow moiré as one of the techniques to be used for those type of measurements [6]. The technique is robust with a diffuse sample surface requirement rather than a specular surface. It can be

implemented with a variety of light sources [7]-[9] . It is also a whole field technique, which allows for characterization of the entire specimen surface at one time. Whole field techniques are better for dynamic system measurements, as the surface displacements are quantified simultaneously rather than over a period of time with point by point measurement. The technique determines absolute displacement from the sample surface to the reference grating which can be utilized to determine relative distances.

Use of shadow moiré on electronic packages is common in the literature, and its use continues to the present [7]-[22]. Some applications included samples placed in solder reflow conditions [17]-[19] and thermal loading of printed wiring boards and other electronic components [10]-[14]. Warpage under thermal treatment, as a result of differences in CTE between the materials in electronic packages, is important, as it can be tied to reliability issues. Conventional shadow moiré on the micro scale could be realized down to 110 μm/fringe, and with the use of the half Talbot distance, the contour interval could be further brought down to 43 μm/fringe [23] with adequate dynamic range. Shadow moiré at non-normal angles has been explored [11], but the angles used were small. An example of shadow moiré, shown in Figure 1.3, details the measurement of a processor undergoing thermal cycling.

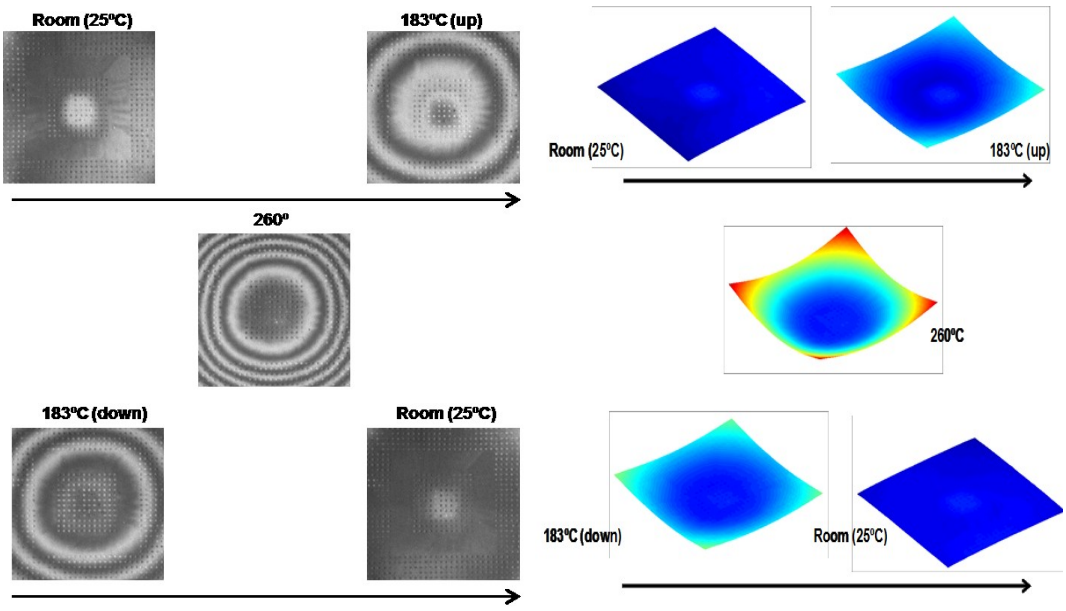

Figure 1.3: Shadow Moiré thermal cycling example

Phase Shifting

An important technique called phase shift is used to increase the overall pattern recognition of fringe based measurement techniques [25]-[30]. The intensity distribution is assumed to be sinusoidal in shape. The intensity distribution of the fringe pattern is then defined as:

$$I(x,y) = I_m(x,y) + I_a(x,y)\cos(\phi(x,y))$$

where I_m is the background intensity,

I_a is the modulation intensity, and

and ϕ represents the angular phase of the fringe pattern;

the ϕ is related to fringe order $N(x,y)$ by $\phi = 2\pi N$. (0.1)

There are three unknowns in the above equation, which means three equations need to be solved in order to determine I_m, I_a and ϕ. At least three fringe patterns with equal phase differences are required to implement phase shifting. The ϕ term is especially important

because it provides information on the points between the fringe patterns. Different algorithms were developed that used more than the requisite three phase-shifted images, since more phase steps smooth out those phase shift errors. The most widely used algorithm takes the information from four images to calculate the phase and is given as:

$$
\begin{aligned}
I_1(x,y) &= I_m(x,y) + I_a(x,y) * \cos(\phi(x,y) \\
I_2(x,y) &= I_m(x,y) + I_a(x,y) * \cos(\phi(x,y) + \pi/2) \\
I_3(x,y) &= I_m(x,y) + I_a(x,y) * \cos(\phi(x,y) + \pi) \\
I_4(x,y) &= I_m(x,y) + I_a(x,y) * \cos(\phi(x,y) + 3\pi/2) \\
\phi(x,y) &= \arctan\left(\frac{I_4(x,y) - I_2(x,y)}{I_1(x,y) - I_3(x,y)}\right)
\end{aligned}
\tag{0.2}
$$

Errors when acquiring the images after phase shift can result in significant deviations from the true phase value. Current research has developed numerical analysis that can apply the phase shift technique even if the phase shift is arbitrary[26] or constant but unknown[28]. It is also necessary to unwrap the phase diagram after the use of the phase shifting algorithm. The absolute value of the phase is lost when the phase range extends over 2π due to the properties of the arctangent function used in its calculation.

A systematic error is introduced in phase shifting techniques by assuming a sinusoidal intensity distribution. In reality the intensity distribution of shadow moiré is a complex function of different experimental parameters [31]-[33]. The error of the 4-image phase shift algorithm was experimentally tested and derived, and known to introduce a maximum error of 1.7% of the contour interval [23] [32]. The error is therefore more pronounced when using a lower measurement sensitivity system. High basic measurement sensitivity is necessary with use of phase shifting.

Summary of Work

There is a need for warpage measurement techniques in the microelectronics industry as packages continue to grow smaller while the designs grow more diverse. To that end, an existing shadow moiré technique is modified to create a framework for taking measurement that will surpass current existing limits dictated by the traditional high-sensitivity moiré setup. The non-coplanarity of the new configuration will solve inherent issues in the conventional setup of shadow moiré regarding the reflection from the grating and widens the viewing angles that are viewable in a traditional setup. The following chapters will be used to illustrate an advanced shadow moiré technique that uses non-standard viewing angles to decrease contour interval size. The new contour interval equation associated with the modified shadow moiré that uses a non-coplanar setup was derived and then experimentally verified. The modified technique was used to demonstrate the improvement in sensitivity for package warpages measurement. Sensitivity improvements at very large angle non-normal values are shown to have the potential of reducing the contour size by half as compared to normal viewing.

Equation Section (Next)

Chapter 2: Conventional Shadow Moiré

Rectilinear Propagation of Light

The shadow moiré technique can be described utilizing the assumption of rectilinear propagation of light. The rectilinear assumption only holds when the distance between the grating and specimen is small compared to the Talbot distance. This grating self-imaging distance will be discussed later in the thesis. The method requires an amplitude grating, a light source, a prepared sample, and an observer, normally a camera, to record the images. The sample is sprayed with a thin layer of white matte paint. The paint allows the sample to uniformly diffuse the visible rays of light and is considered thin enough to not significantly alter the out-of-plane displacement.

The grating required is the Ronchi grating. It is a series of alternating transparent and opaque bars of equal width; the physical grating is typically made by depositing the metal pattern layer on one side of a glass plate. The flat grating has to be placed so that the bars are perpendicular to the imaging plane. Previous researchers have used Ronchi type flexible [34] and non-flat gratings [35] for specific applications; this thesis will solely be using flat glass gratings. As stated previously, a variety of light sources can be used. The typical light source is a bright white light with a small size, approximating a point source or a slit that is parallel to the grating lines.

The light source illuminates the grating, which casts a shadow grating on the specimen surface. The camera captures the interference between the shadow grating on the sample

and the superimposed reference grating, producing a moiré fringe pattern. For a pinhole aperture, there is only one light beam which will be scattered from the surface that will reach the observer. The interference pattern is equivalent to a contour map, the number of fringes between two points indicate the out of plane displacement between the points.

The concept behind the technique is shown in Figure 2, with the setup having the following variables: z is the displacement between the reference grating and the specimen surface; g is the reference grating pitch, α is the illumination angle, and ψ (or β) is the incident light to the camera angle. Example of how the fringes look at the different points can be seen. The first point of interest is point A. As the light passes through the grating and reaches the observer, that point is seen as a bright fringe. Point A is assigned the zero fringe order, as there is zero distance between it and the grating. Similarly points E and C are seen as bright fringes. Points B and D are dark fringes as the light diffuse from the surface interferes with the dark part of the grating; a dark fringe would also occur if the source light has interference with the dark part of the shadow fringe. The fringe order can be determined by the number of fringes between the entrance of the light and the exit of the light. A full fringe is the distance between one bright fringe to the next. In the case of point C, there are four fringes between point A (the zero reference) and the light entrance. There are three fringes between point A and C, the point where the observer sees the light passing through the grating, meaning that point C has a fringe order of one.

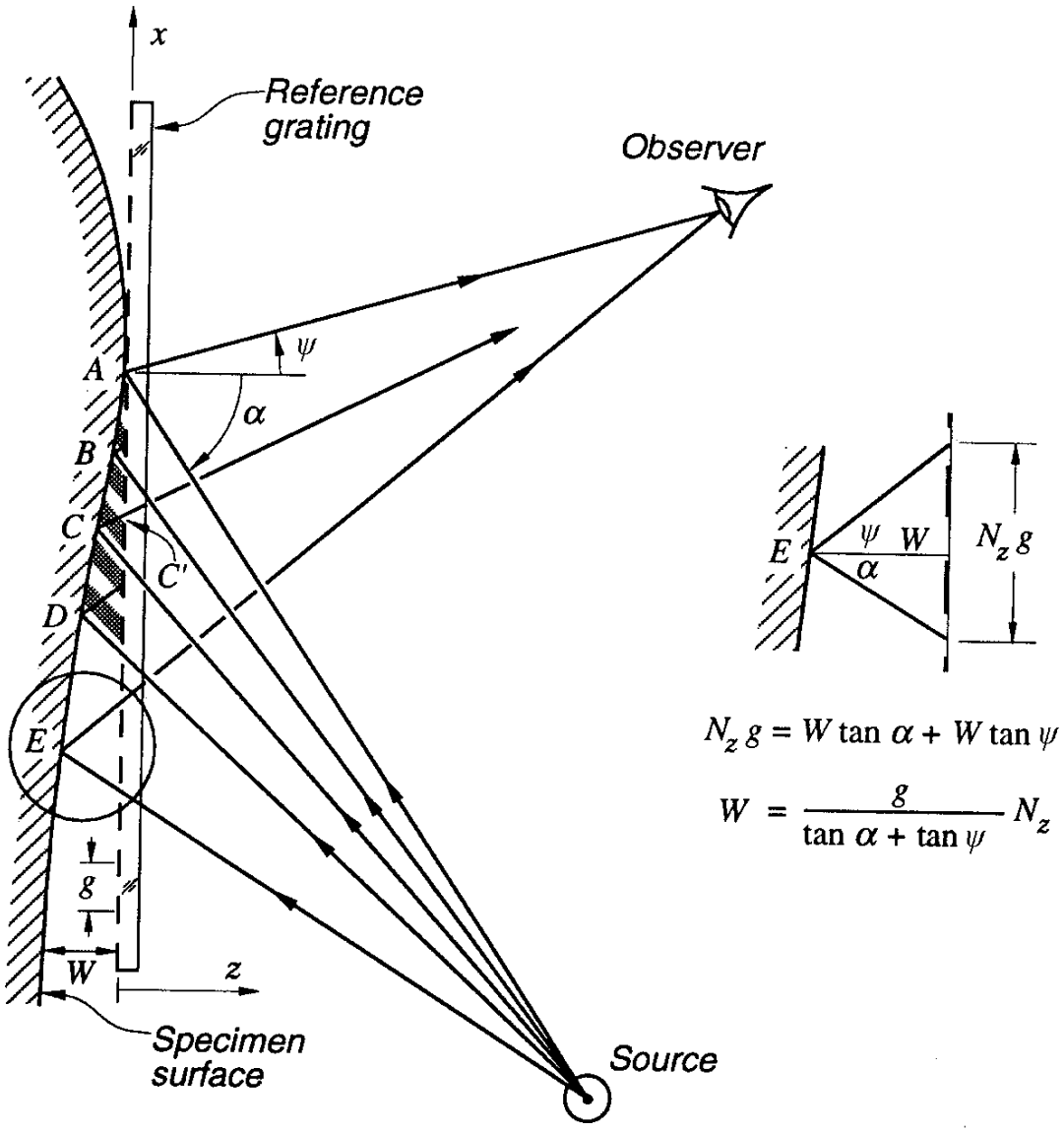

Figure 2.1: Rectilinear Demonstration of Shadow Moiré [36]

From geometry, the relationship between z and the fringe order N is determined as:

$$z(x,y) = \frac{g}{\tan(\alpha)+\tan(\beta)} N(x,y) \tag{1.1}$$

Note that the sensitivity is not constant across due to the specimen as the angles are constantly changing at every point. A solution to achieving constant sensitivity can be seen in equation 2.1. The two ways to achieve constant sensitivity would be to keep tan(α)+tan(β) constant or keep the angles the same at every point. A method to achieve the theoretical constant sensitivity by keeping tan(α)+tan(β) constant is to place the light source and observer the same distance away (L) from the reference grating plane [36]. It can then be approximated that

$$\tan(\alpha)+\tan(\beta) = \frac{D}{L+z} \approx \frac{D}{L} \tag{1.2}$$

where D is the distance between the light and the observer.

The approximation in equation 2.2 allows the z displacement at every point to be correlated directly to the fringe order. Combining equation 2.1 and 2.2, the constant contour interval, which is the amount the fringe order is multiplied by, can be then calculated as:

$$\Gamma = \frac{g}{\tan(\alpha)+\tan(\beta)} = \frac{g}{(\frac{D}{L})} = \frac{L*g}{D} \tag{1.3}$$

The assumption inherent in this approximation is that the range of displacement across all the points is much smaller than the L distance. The previously described method for constant sensitivity for the fringe patterns is shown, with oblique angle viewing in Figure 2.2a and normal viewing in Figure 2.2b.

The second method to achieve constant sensitivity, but not pursued in this thesis, is to keep the angle constant at all points by the use of collimating lenses (as shown in Figure 2.3). The divergent light from the source will be collimated onto the sample surface so it hits the sample at a specific α. The diffuse light from the specimen would then be observed through a collimating lens as well, resulting in a known constant β. The use of this version of shadow moiré would not be constrained by any distance requirements for source and observer placement; however the sample size is limited to the size of the collimating lenses used.

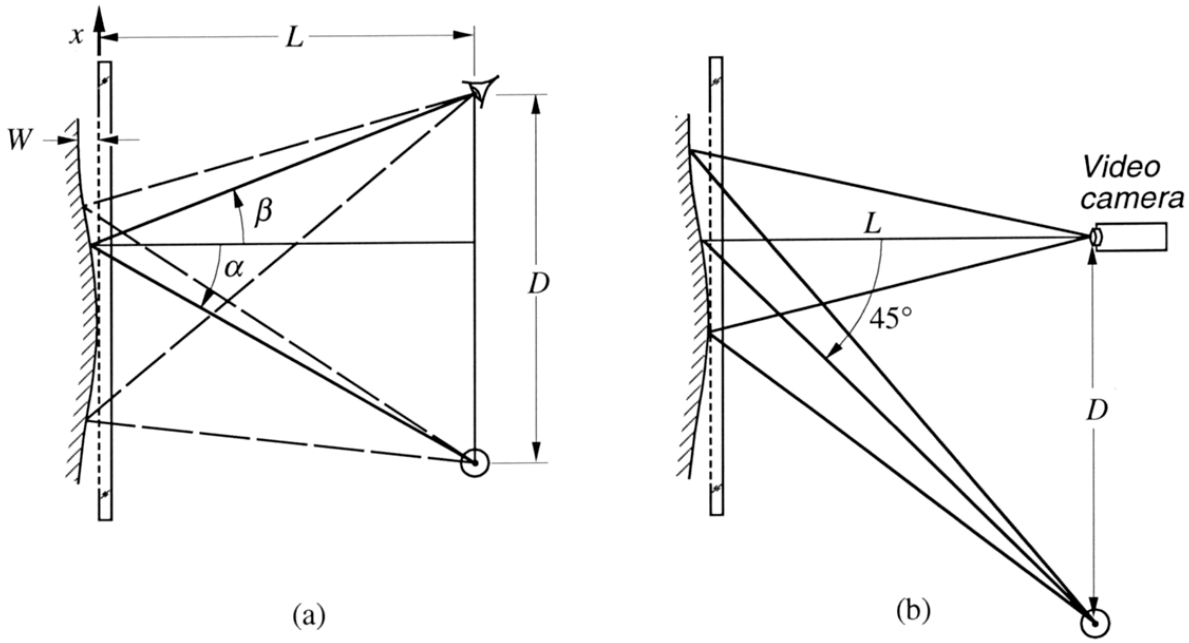

Figure 2.2: Constant sensitivity configuration for shadow moiré by keeping $\tan(\alpha)+\tan(\beta)$ constant, (a) oblique viewing, (b) normal viewing [36]

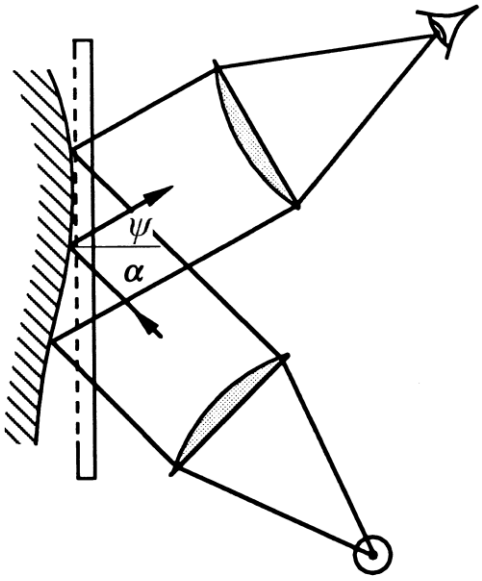

Figure 2.3: Constant sensitivity with collimating lenses at oblique angles [36]

Normal viewing is popular in shadow moiré configurations because there are no visual distortions of the sample during viewing. However, in order to have the large values of α at normal incidence, the light placement gets progressively further away. This becomes a practical setup problem as well as light intensity decrease the further away from the source it is. Reflection from dielectric surface also means less light is being transmitted through the grating, which is also limiting the intensity of the light beam that the camera is picking up. A practical limit of tan (α) = 3 was suggested for normal incidence to have usable light intensity.[23]

Diffraction: Talbot Distance and its impact in Shadow Moiré

The equation for shadow moiré seems to indicate that the fringes will appear at any displacement. In reality, the fringe contrast changes based on the sample's distance away from the reference grating. The fringe contrast is affected by the Talbot effect, a grating self-imaging effect that occurs due to diffraction from a periodic structure. The

illuminated reference grating splits the light beam into multiple diffracted beams. The diffracted beams will then interfere with each other, producing a virtual grating at a specific distance that is the same pitch as the reference grating. Those virtual gratings are called "Talbot images," with the replication occurring at the Talbot Distance (TD). The TD equation for normal incidence is:

$$D_T = \frac{2g^2}{\lambda} \quad [36] \tag{1.4}$$

For shadow moiré, the TD based on oblique illumination was given by Testorf as:

$$TD^{\alpha} = \frac{2g^2}{\lambda} * cos(\alpha)^3 \quad [38] \tag{1.5}$$

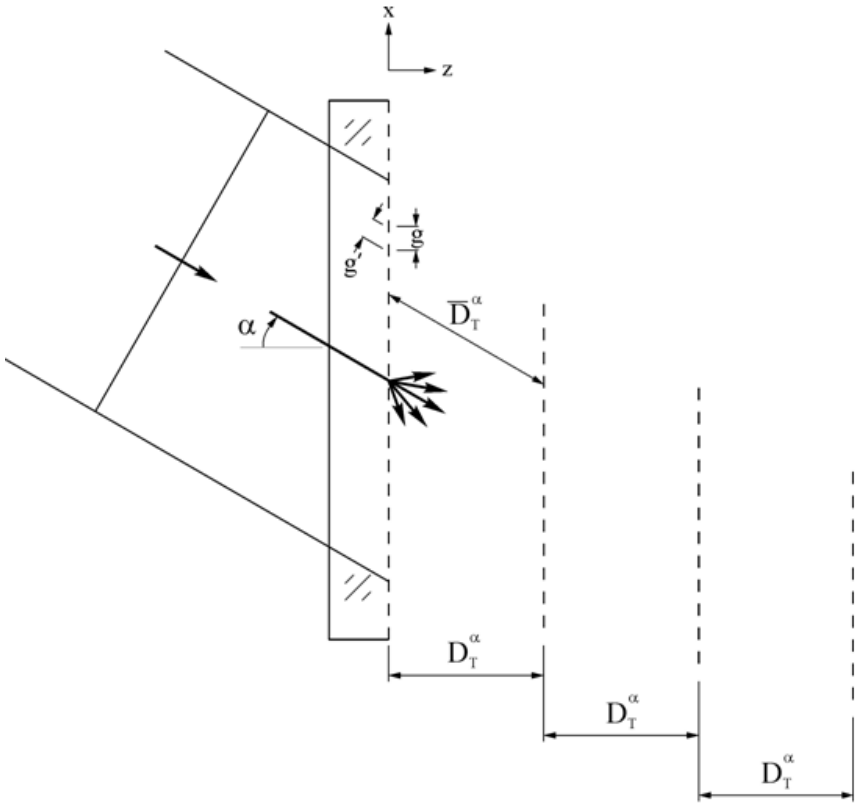

Figure 2.4: Illustration of Talbot distance for oblique illumination with complimentary virtual gratings at multiples of ½ the Talbot distance [37].

A simple geometric derivation of Talbot distance can also be utilized to describe the interaction of the diffracted beams [37]. When collimated light enters the grating at an angle of α, defined perpendicular from the grating bars, the effective grating is

$$g' = g\cos(\alpha) \tag{1.6}$$

From equation 2.3, the distance between the grating and the virtual grating is:

$$\overline{TD}^{\alpha} = \frac{2g'^2}{\lambda} = \frac{2(g\cos(\alpha))^2}{\lambda} = \frac{2g^2}{\lambda} * cos(\alpha)^2 \tag{1.7}$$

The distance of the virtual grating parallel to the grating surface is calculated to be:

$$D^{\alpha} = \overline{TD}^{\alpha} * \cos(\alpha) = (\frac{2g^2}{\lambda} * cos(\alpha)^2) * \cos(\alpha) = \frac{2g^2}{\lambda} * cos(\alpha)^3 \tag{1.8}$$

The equation is equivalent to the equation derived in reference [38], which utilized a mathematical derivation of off-axis light diffraction through a Ronchi grating. This equation was used to calculate the TD from 45° to 63° with two different pitches, shown in Figure 2.5. It can be seen that both the decrease of grating pitch and increase of α greatly affects the TD. The increase of sensitivity through those two means are constrained by how quickly the Talbot distance is modified.

It is known that complimentary images of the grating appear at ½ TD, while at ¼ and ¾ TD a destructive interference virtual grating will occur [37]. Therefore, at the ¼ and ¾ TD, the virtual grating will cause the contrast to go to zero. Example of self-imaging is shown in Figure 2.6. The TD is proportional to the grating pitch squared, from equation 2.4, so decreasing the gratings pitch quickly results in very small usable distances. Note that the TD is not dependent on the β angle, so any gains in sensitivity from using the β angle will not hinder the contrast of the technique based on diffraction.

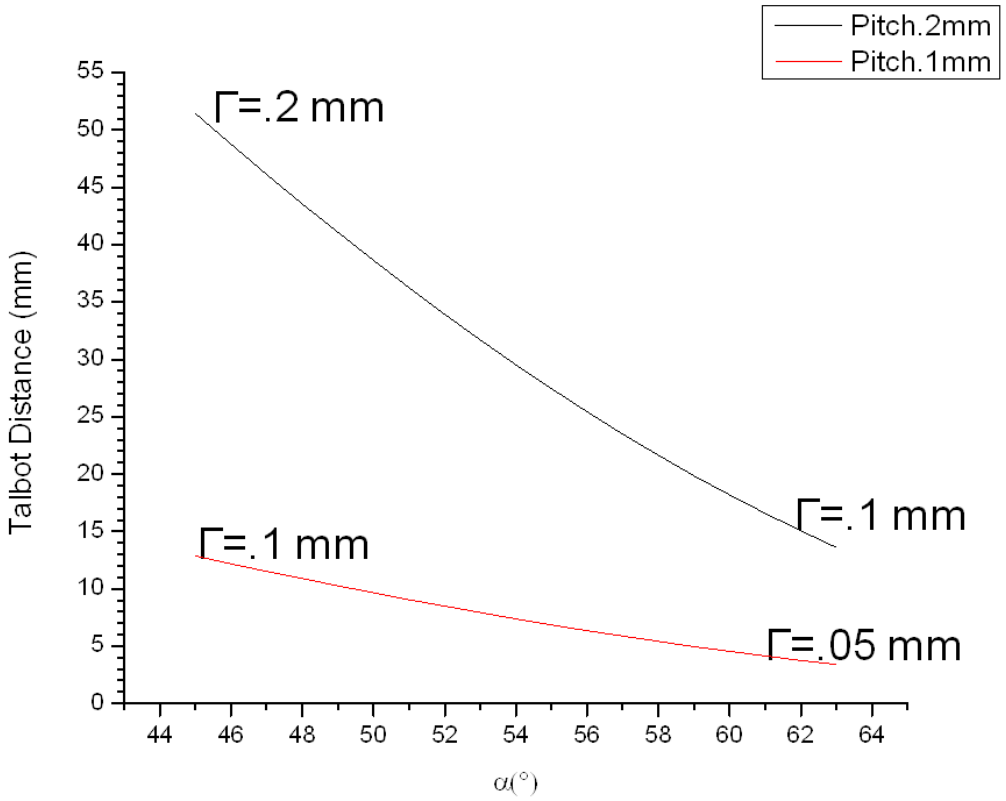

Figure 2.5: Calculated Talbot distance for range of 45-63°, pitch of 0.1 and 0.2 mm

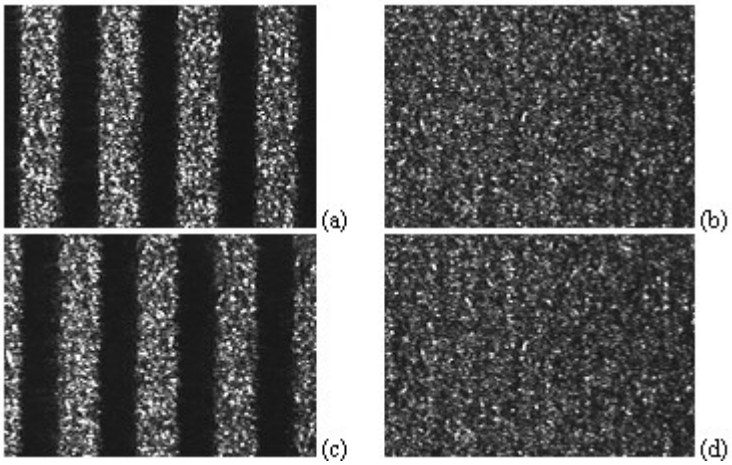

Figure 2.6: Self-imaging of 10 line/mm Ronchi gratings at n-talbot distance where n is equal to a) 0, b) ¼, c) ½ , d) ¾ [37]

The dynamic range of the technique is dependent on the magnitude of the TD; a larger TD means a larger dynamic range, assuming that the TD is the constraint. The knowledge of the dynamic range is crucial as measurements of deformation outside of the dynamic range can result in fringe disappearance. An example of this is shown from [23], where there a clear areas where the fringe is no longer visible.

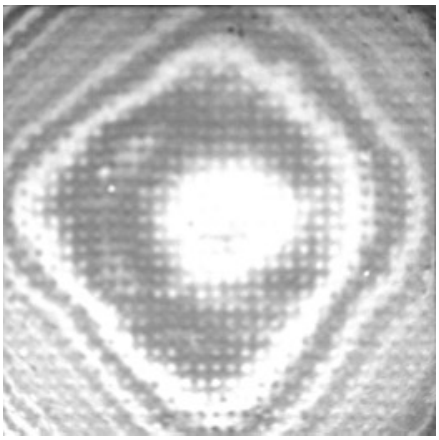

Figure 2.7: Warpage of flip chip BGA with g=0.1mm and α=63° for a 50um/fringe contour interval [23]

To balance the grating pitch and the alpha angle, a relation was found between the contour interval and the TD. By combining equation 2.1 and 2.6, the TD relation to the contour interval is:

$$TD^{\alpha} = \frac{2\Gamma^2}{\lambda} * cos(\alpha)^3 * (\tan\alpha + \tan\beta)^2 \tag{1.9}$$

The critical angle can then be found by differentiating Eq. 2.7 with respect to α. An assumption of β = 0 was used as the Talbot distance is not dependent on β:

$$\begin{aligned} \frac{\partial TD^{\alpha}}{\partial\alpha} &= \frac{2\Gamma^2}{\lambda} * \frac{\partial}{\partial\alpha}(cos(\alpha)^3 * \tan(\alpha)^2) \\ &= \frac{\partial}{\partial\alpha}(\frac{\Gamma^2}{\lambda}\sin 2\alpha \sin\alpha) = \frac{\Gamma^2}{\lambda} 2\sin\alpha(3\cos^2\alpha - 1) = 0 \end{aligned} \tag{1.10}$$

The value that solves Eq. 2.8 is $\alpha_c = 54.7°$, from [23]. This means that utilizing angles near that angle will also result in the highest Talbot distance with the corresponding grating size for a specific contour interval. However, the function shows there is a limit to the α useable in the higher angle region due to TD.

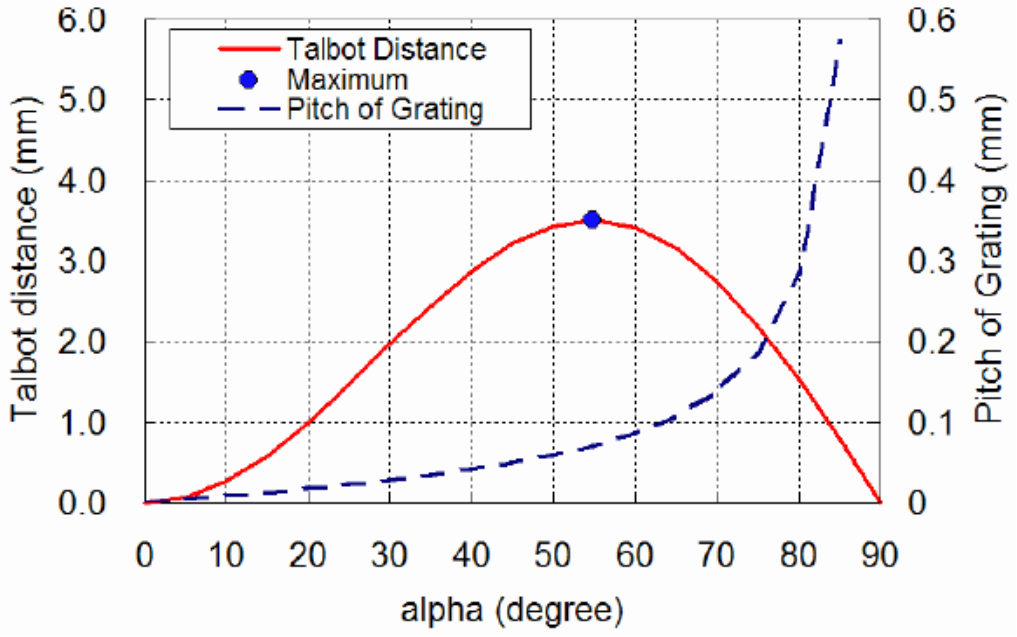

Figure 2.8: Talbot Distance for contour interval of 100um/fringe with β = 0° [23]

Previous work ([23]-[3], [39]-[40]) utilized the shadow moiré at distances other than the zeroth distance in order to take advantage of the increase in dynamic range. At the zeroth order, the maximum dynamic range before contrast goes to zero is only ¼ TD. Since there is a complimentary image at half TD, placing the samples at that location expands the dynamic range from ¼ to ¾ TD. In practice, the constraints for the half TD are still α and grating pitch.

Constraint of incident angle and grating due to contrast

In order for fringe pattern techniques to work, a visually distinctive pattern is required; therefore, the contrast between the dark and light fringe patterns is an important constraint for the shadow moiré technique. Previously, Han et al. derived and verified equations for the contrast of shadow moiré patterns at different displacements from the grating [39]. Equations for fringe contrast in shadow moiré were also established for a laser light diode source and a white light. It was determined that the virtual grating and the aperture of the camera lens are the two major factors that affect the contrast of moiré pattern. The virtual grating depends on the Z displacement, the Talbot distance, and the secondary Talbot distance. The aperture of the camera lens has an impact on how the light gets captured in the camera.

From equation 2.6, it can be deduced that the light source's properties play a large role in the virtual grating. The contrast is dependent on the spectral bandwidth and the wavelength of the light source itself [23]-[3]. Contrast consideration also limits the possible placement of the specimen due to the limitations of the dynamic range.

The aperture of the camera affects the contrast and produces another limiting effect when certain camera setups are used. In a purely theoretical configuration, the camera would have a pin-hole aperture, and the only light entering would be that exiting the grating. In practice, it is possible for the camera to pick up some light being scattered by light exiting the grating. With this secondary light source, the dark fringes will become slightly brighter, thus decreasing the contrast. Figure 2.9 illustrates this.

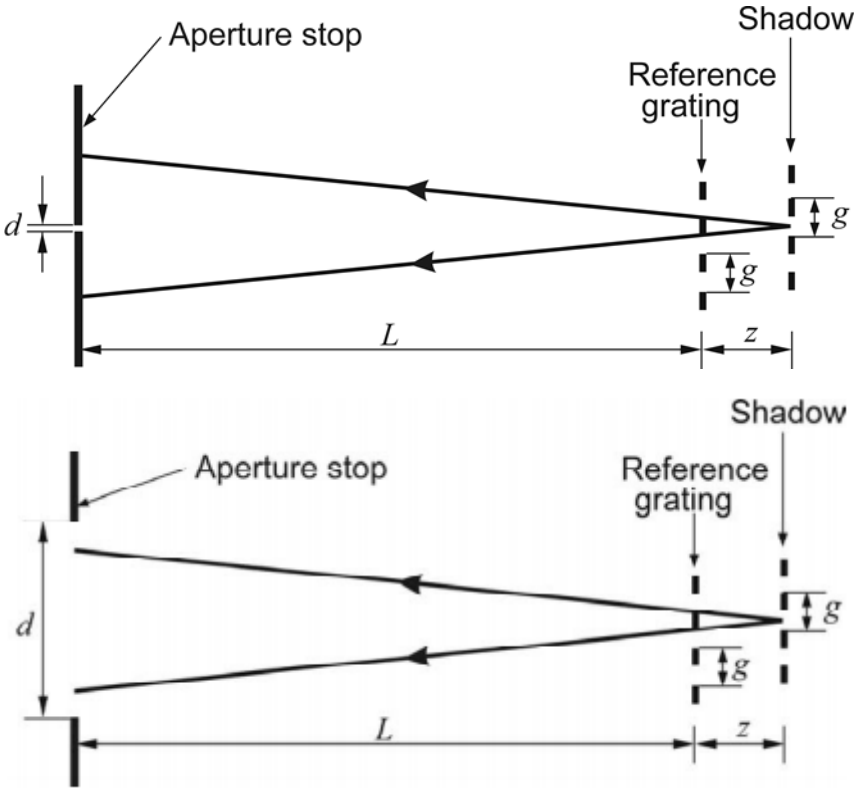

Figure 2.9: Aperture effect: (top) pinhole aperture (bottom) large aperture [3]

Smaller apertures will decrease the contrast less by decreasing the amount of secondary light coming into the camera; however, apertures too small will receive too little light, resulting difficulties in detecting fringes. Reference [41] mathematically determined the intensity of the shadow moiré based on the pitch and aperture size. The max and minimum intensity, respectively, is given for a circular aperture as:

$$I_{\max} = I_{input}\left(\frac{1}{2} - \frac{2dz}{3\pi gL}\right), I_{\min} = I_{input}\left(\frac{2dz}{3\pi gL}\right) \tag{1.11}$$

With increasing distance between the grating and sample, the max intensity and minimum intensity will eventually be equal; at that point, the washout distance, the

contrast is zero regardless of any effect. The contrast due to a circular aperture can then be calculated through:

$$C_a = \frac{I_{\max} - I_{\min}}{I_{\max} + I_{\min}} = 1 - \frac{8 d_e z}{3 \pi g} \tag{1.12}$$

where d_e is the aperture diameter/distance from the camera [23]. The term d_e, the effective aperture, allows a more realistic determination of the size of hole that light will get through to the camera.

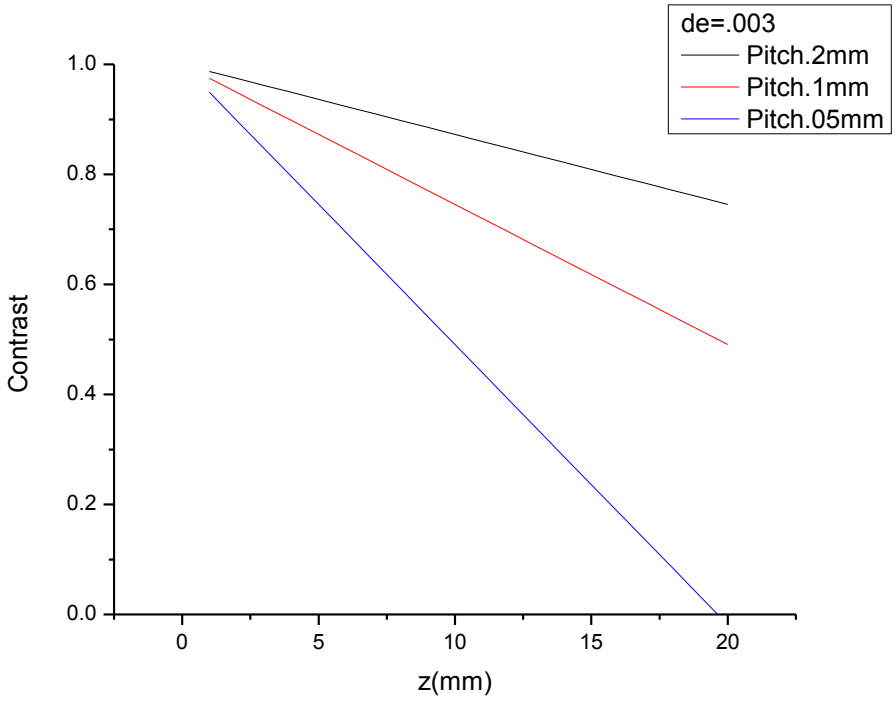

Figure 2.10: Contrast due to aperture effect for d_e=.003

From equation 2.4, smaller effective aperture, larger grating pitch, and appropriate specimen placement will produce higher contrast. Grating pitch needs to be kept sufficiently small in order to gain desired sensitivity in measurement. However, as shown in Figure 2.10, decreasing grating pitch means worse contrast due to the aperture effects.

The grating is a limiting factor for increasing sensitivity and will be kept at smallest 0.1mm for typical applications.

Limitation of oblique viewing angles

Due to the constraints limiting α and grating pitch, the usage of the β angle to improve sensitivity is the next step. The choice to stick with normal viewing comes from the distortion that is introduced with non normal viewing. The visual distortion is a linear distortion along the direction of the imaging plane. For example, a simple square shape will have its length along the direction of the imaging plane shrink by cosine β. Figure 2.11 shows the image of a square sample, where the left image is shrunk along the horizontal direction due to the β angle.

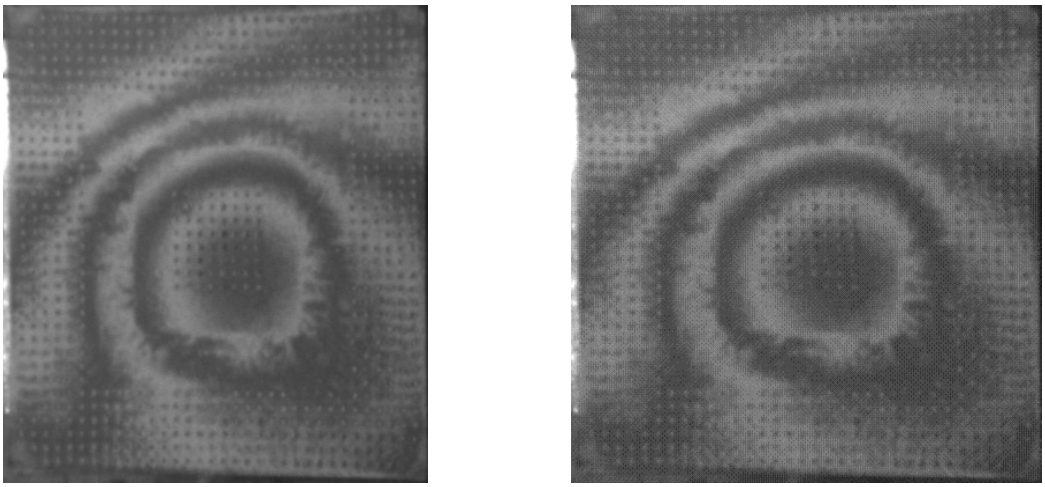

(a) (b)

Figure 2.11: Fringe patterns of α = 63°, β = 25°, g=0.1 mm , (a) unmodified

(b) Stretch correction to have square specimen

From the governing equation it would appear that all angles of α and β are viable. However, light reflection and diffraction issues come into play at specific angle

combinations. The grating surface is a dielectric, so a portion of the incident light will reflect off from the surface. At higher incident angles, the intensity of the reflected light grows larger. The reflected light off the grating will exit at the incident angle. Therefore, if the camera is placed in or close to the reflected light's path, the reflected light's intensity would dominate the light contribution from the diffuse scattered light coming from the specimen. This would result in the lightening of the dark fringe; or, in the worst scenario, the saturation of the camera's sensors as can be seen in Figure 2.13. Thus, if the camera is placed at an angle approximated to the reflected angle of the light source, the fringes could potentially disappear.

Assuming the system is coplanar, there are two possible areas outside of the reflected beam's path to place the camera. Figure 2.12 shows the potential light paths of the reflected light, with the orange colored area representing the reflected light. The camera would have to be placed either above or below where the reflected light is propagating. Large β angles result in distortion of the specimen image and a similar issue to α with the camera distance being too long. At small β angles, distortion is negligible; however, $\tan(\beta)$ is close to zero, and there would not be significant improvements of sensitivity from normal incidence. With the above cited concerns/limitations, neither of these two camera locations is acceptable for use to improve sensitivity. Therefore, a change in the setup has to be made in order to access the angles normally unviable.

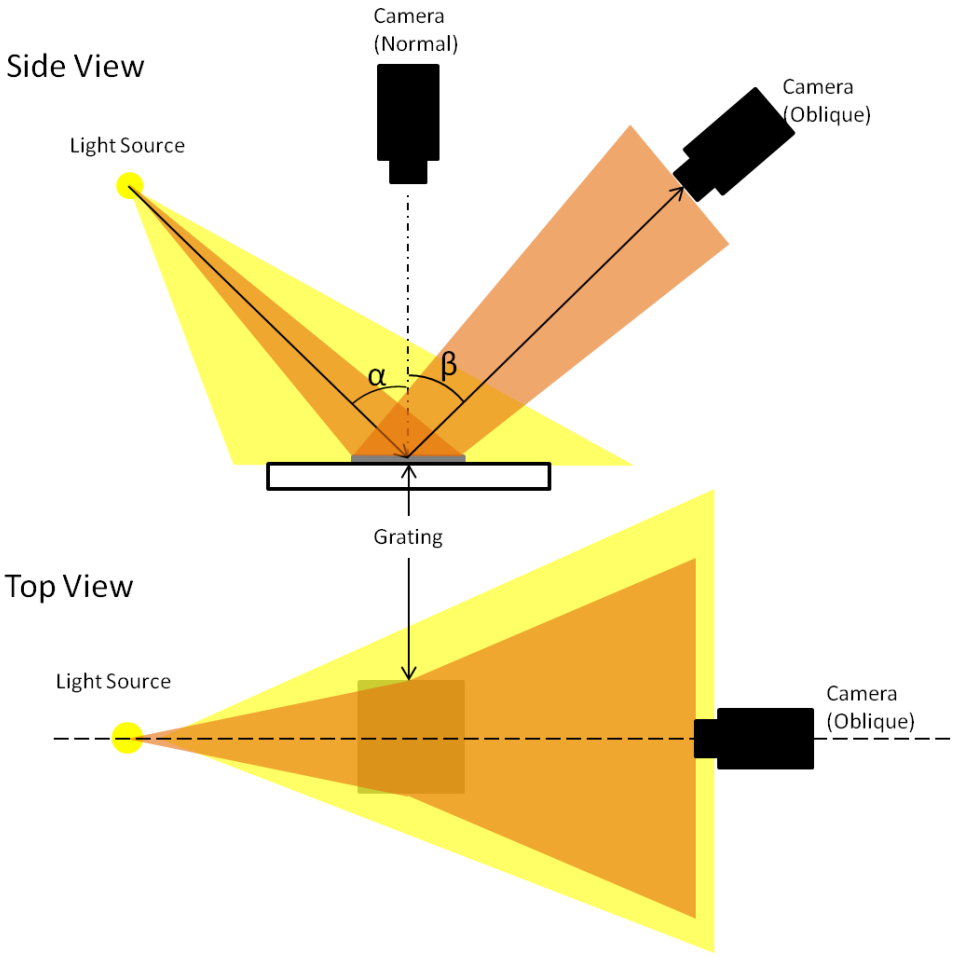

Figure 2.12: Light paths for shadow moiré with non-zero beta

Figure 2.13: Reflection captured at α=63°, β=60°, g= 0.2mm

Chapter 3: Advanced Shadow Moiré Technique

Shadow Moiré using Non-conventional angles

Due to the issues associated with using oblique viewing at certain angles for traditional shadow moiré, a modification to the technique is proposed. This advanced technique introduces a rotation of the components in relation to the initial visual plane. The system positioning is shown in Figure 3.1. The configuration introduces two new angles: one affects the light source (θ), while the other affects the camera (γ). Both angles are defined between the original main axis and the subsequent light or viewing path axes. The two angles are introduced so the reflected light will be directed away from the camera. The shadow moiré technique still applies as sufficient light that diffuses off of the specimen will be captured by the camera.

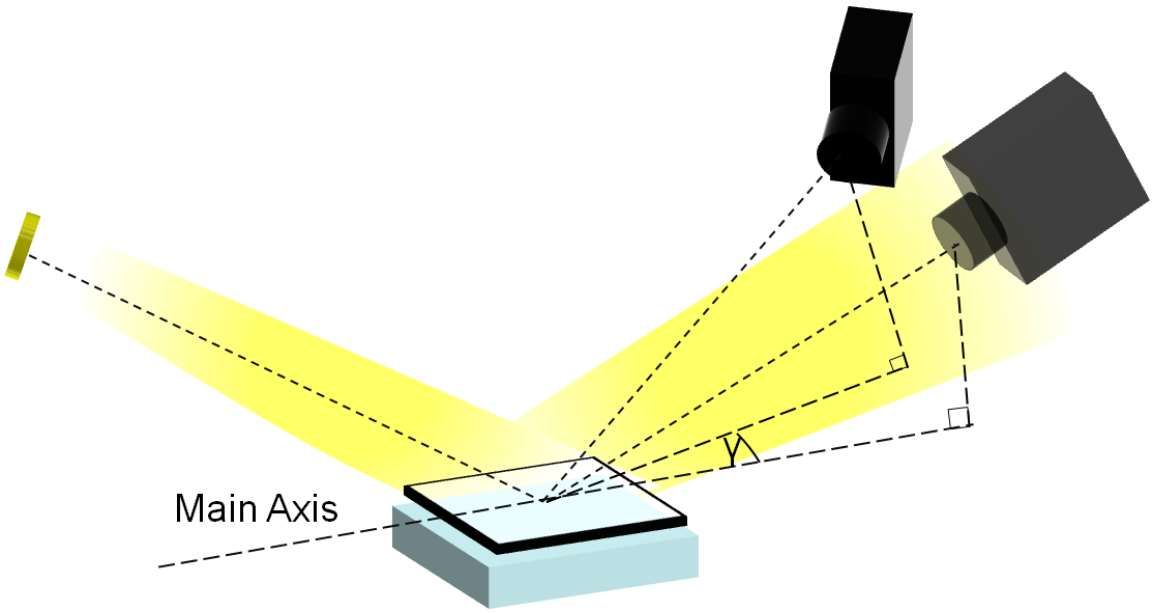

(a)

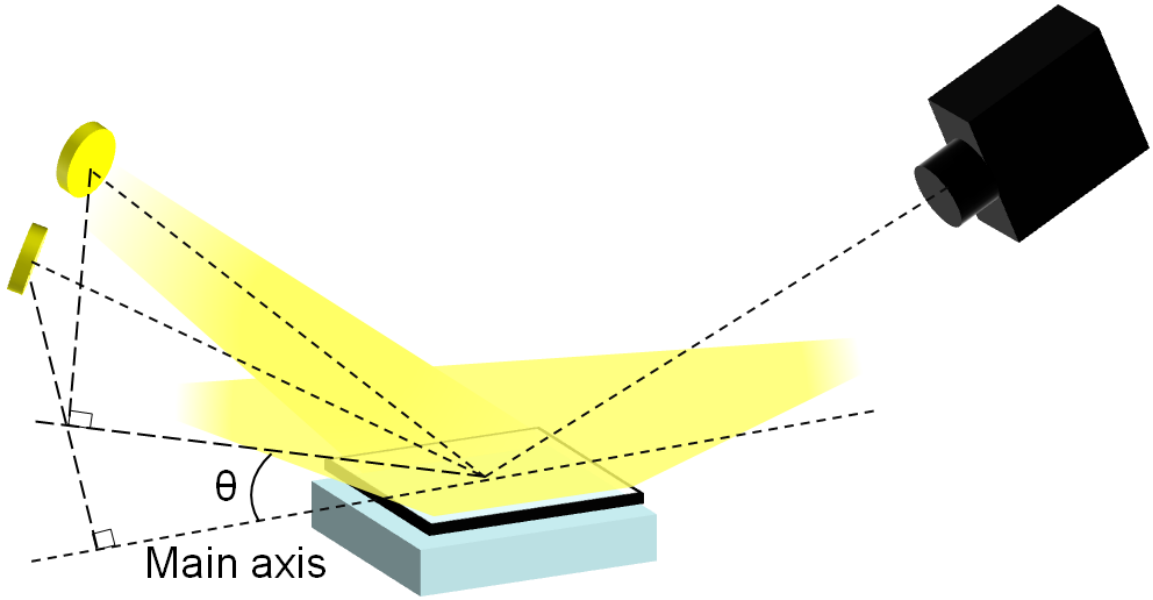

(b)

Figure 3.1: Proposed Shadow Moiré Configuration a) Rotated camera b) Rotated light source

The governing equation for this new system is obtained from projecting the light vector and the viewing light vector onto the main plane. The component of the light in the viewing plane is obtained by multiplying the light vector by cos(θ) or cos(γ), depending on which component was rotated. Even if both were rotated, the fringes between the light entrance and exit would still be N*g, as seen in Figure 3.2. The horizontal value, and subsequently the z displacement, could be calculated as:

$$z * tan\alpha\, cos\theta + z * tan\beta\, cos\gamma = N * g \tag{1.13}$$

$$z = \frac{g}{tan\alpha\, cos\theta + tan\beta\, cos\gamma} N \tag{1.14}$$

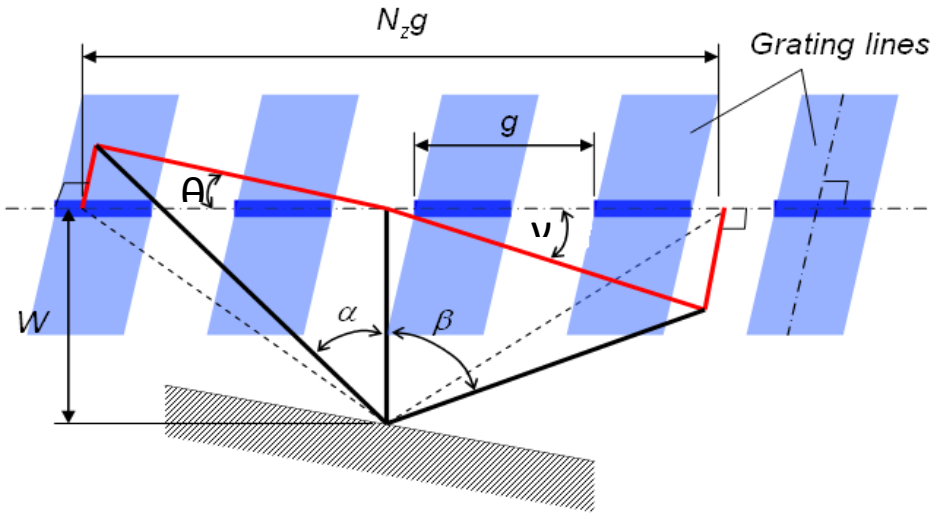

Figure 3.2: Geometric side view of modified technique

By introducing the rotational angle, the amount of light decreases as tan(α) gets larger, and the rotation will always decrease the overall sensitivity. Therefore, non-coplanar viewing should only be used at β angles for which the oblique configuration could not be achieved due to light effects in a coplanar setup. In addition, only the camera or the light source should be rotated but not both, because the rotation of one already solves the

problem posed by reflected light. Having both components rotated will unnecessarily diminish the sensitivity.

Theoretically, rotating either the light or the camera should have a similar effect on the contour interval. However, in practice, moving the camera adds one more rotational distortion to the image on top of the horizontal shrinking already introduced by the oblique viewing. The additional rotational distortion will necessitate image processing software to reorient and convert the non-normal viewing image to normal viewing. Therefore, the focus of the advanced technique under investigation will be on the positioning of the non-coplanar light source with a coplanar camera to avoid introducing the extra rotational distortion.

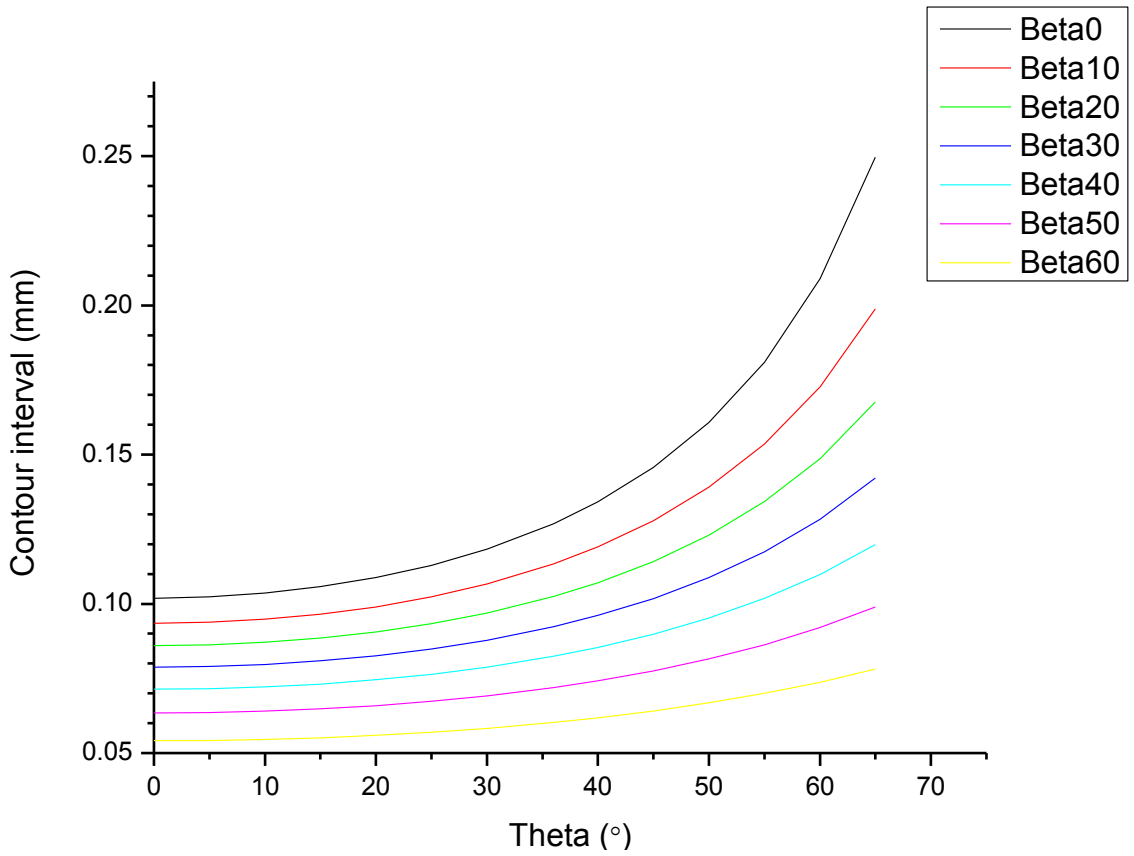

Figure 3.3: Theoretical contour interval values at α=63°, g=0.2mm

From the theoretical derivation, it can be surmised that when the camera is placed at a large angle of β, additional increases to the β angle does not decrease the contour interval linearly. A high γ angle can undo the gains from using the β angle, with more of an effect when the β angle is set smaller. However, the contour interval changes slightly for small γ angles when compared to the normal configuration. The small increase of contour is due to the non-linearity of the cosine function in the derived formula. For example, a γ angle of 20° still results in a contribution of 0.94 of the α term. The use of the modified technique should be limited to cases that need to avoid the reflection and that the rotation should be kept as small as possible.

Implementation Verification

Experiment Configuration

As stated previously, the proposed technique requires a light source, observer/camera, and reference grating. The setup has a mobile light source and camera for easy adjustment in order to attain the necessary angles during the experiment. Both the camera and the light source were placed on a rotation stage, which was then subsequently attached to a magnetic base. The setting of each individual rotation stage determined the α and β angles. The magnetic bases were then placed so that the center of each component was at the desired angle from the sample surface. An illustration of the placements can be seen in Figure 3.4.

Either the grating or the sample has to be vertically translatable for phase shifting to work. In this configuration, the sample is stationary, and the grating is attached to a holder on a servo motor. The change in L will slightly affect the sensitivity between phase-shifted images; as previously assumed the displacement is negligible in comparison to the distance that the camera and light are placed.

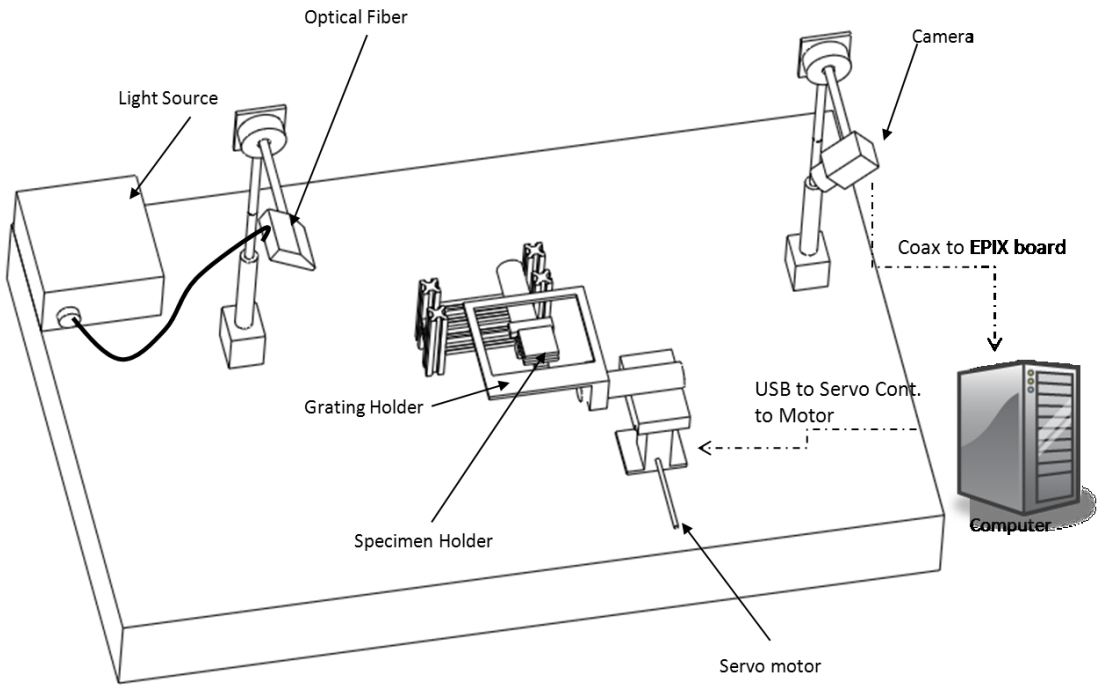

Figure 3.4: Illustration of Modified Shadow Moiré setup

The contour intervals associated with the configuration were determined by comparing a reference image to an image taken after a known out-of-plane grating shift. A grating movement equal to the contour interval results in the fringes moving one fringe order. Utilizing this fact, moving the grating to values close to the estimated contour interval will result in fringes. The different fringes are then compared to the fringes from the original grating setting by finding the absolute difference between the corresponding pixels in the fringe images. Plotting the absolute difference found for the images versus grating displacements will result in a valley at the desired range of contour interval. An exact match will not be found due to the contrast change at further distances, hence the use of the smallest difference as the contour interval indicator.

The acquired images were not compared to the same original position image. As a precaution against the sample moving or the grating not moving exactly back into the original position, the images were taken in pairs. The first image was at the initial grating position and the second was the image after grating movement. To prevent backlash, the servo was moved slightly back past the original position and then moved forward into the desired position. Therefore, all grating movements to the desired positions were approached in the direction of increasing displacement.

Theoretically, two images taken in the same configuration should result in an absolute pixel difference of zero. In practice, this is not the case due to random noise. A background noise level was taken to ensure that the difference between the image pairs were significant. Prior to the experiment, two average images were taken at the initial grating placement and compared. The absolute difference between the two images was the background noise value. If the absolute differences in the acquired image pairs was less than the noise difference than the change was deemed too small

Hardware/Software

The light source was a 150W white light (Fiberoptic Systems, Inc. model 1060-150W) with a 2.375 inch line source attachment. The experiment was placed in a dark windowless room in order to eliminate background light. The magnitude of light intensity is adjustable, but was kept at maximum intensity to ensure consistent light intensity. As previously stated, a small aperture means less light entering the camera, so a high intensity light would be needed to achieve the desired contrast.

The camera used was a Pulnix TM-7CN, a ½" format CCD camera with pixel arrangement of 752 (H) x 582 (V) with a zoom lens. The camera was connected to a frame grabber installed on a computer (PIXCI sv4 board). XCAP 2.2 was the software associated with the frame grabber that was used for image acquisition and processing. The images used for the fringe analysis and amplitude comparisons are a composite image composed of the average of twenty images to avoid camera noise. The averaging eliminates random high frequency noise that occurs with taking a single measurement.

The grating holder setup was attached to a vertical translation stage to allow for fringe shifting. The NPZ-1/2 vertical translation stage from JA Noll was actuated by a Thorlabs Z625B servo motor. The vertical translation stage has a two-axis tilt platform to allow for leveling of the grating. The control of the servo was through the Thorlabs DCS-P110 board with the commands sent through the Thorlabs Advanced Positioning Technology (APT) software. The stage has a horizontal to vertical ratio of two to one; the servo displacements reading from the APT software are double the actual movement of the grating holder. Therefore, for one full phase, the displacement required was double the contour interval.

The sample holder is rigidly mounted to the table and the height of the specimen holder could be manually configured. Similar to the grating holder, it incorporates a two-axis tilt platform to level and tilt the sample. In this way, both holders can be configured to be initially parallel to each other and then induce a specific rigid body deformation. The

sample holder was with a small gap between the grating and the sample. The sample cannot be placed touching the grating, since fringes would be affected. Having the grating touching the sample will introduces an extra constraint to the system, which invalidates the results of the experiment.

Verification of the Governing Equation

To prove the new configuration's derivation is correct, the first step was to tune the α angle with the camera at normal incidence. The sample used was a glass slide that was painted on one side to ensure that the specimen was initially flat. The grating and the specimen holder were both leveled through the use of the 2-axis stages to ensure that the fringes seen on the sample came solely from the difference in displacements of the sample and not from any rigid motion from the set up. A bar fringe pattern was then created when the sample holder was tilted in a single direction. The light source was rotated to the desired angle and then moved until the contour interval reflected the original equation's derived value. To ensure the same α angle, the distance away from center of the light source to the sample was kept the same while moving the light source to test the different θ angles.

In order to show the trend, the light was rotated to four different θ angles. The contour interval was determined using the previously described method of comparing images after grating movements to their original grating position image. As part of that analysis, an area of interest was selected to be compared since the sample is only a small part of the image. Since the camera does not move, the sample's location in the capture image

does not change. Since the sample image is a rectangle, the region of interest is a square. The same pixel placement values were used when checking the same configurations.

The first test had the camera at normal viewing incidence with a set α angle of 40° (Figure 3.7). Subsequent trials utilized a different α angle (45°) and β angles (20° and 30°). Examples of the image comparisons for this test are shown in Figure 3.5 and Figure 3.6. The top images are the initial images with the second row corresponding to images after different movements of the grating. The middle image of Figure 3.5b shows the fringe that closest approximates the initial image. The first image shows fringes that have not moved far enough to be in the initial fringe's location. The third image shows fringes that have moved further than the original fringe's position. Therefore, the movement that yielded the middle image is determined as the measured contour interval.

The increase in the contour interval size can be readily seen with the fringe pattern when comparing Figure 3.5 and Figure 3.6. The former has 2.5 fringes on the glass specimen while the latter, with a large rotation angle, shows closer to 2 fringes. As seen from Figure 3.7-Figure 3.10, the measured value followed the trend of the expected values. With increasing θ angle, the contour interval grew larger which is especially pronounced after the 45° mark.

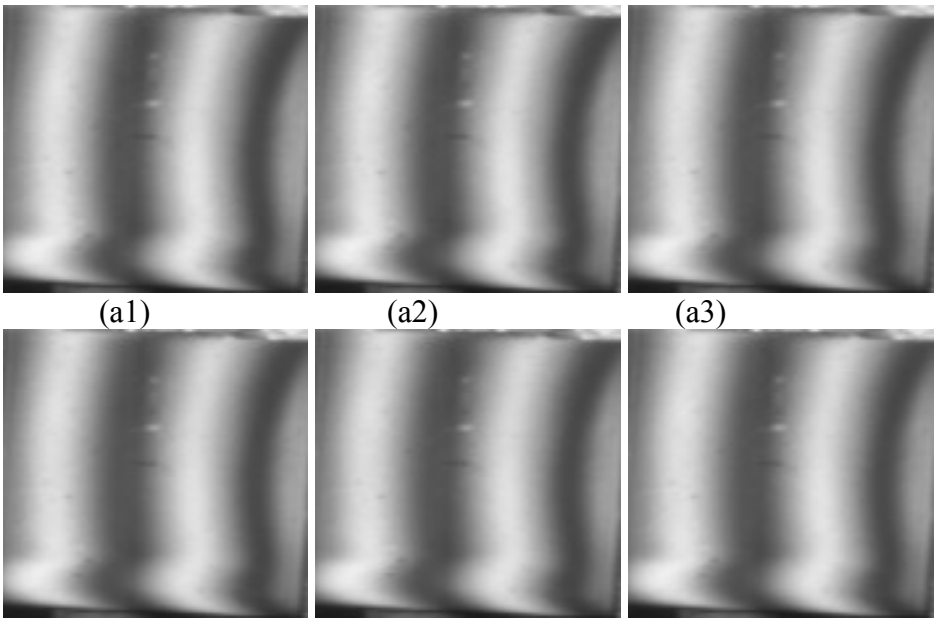

(a1) (a2) (a3)

(b1) (b2) (b3)

Figure 3.5: Image pairs (a) Fringes for α=40°, β=0°, θ=0°, g= 0.2 mm at starting position

(b) Fringes after contour interval of (1)0.236, (2)0.238, (3) 0.240 (mm)

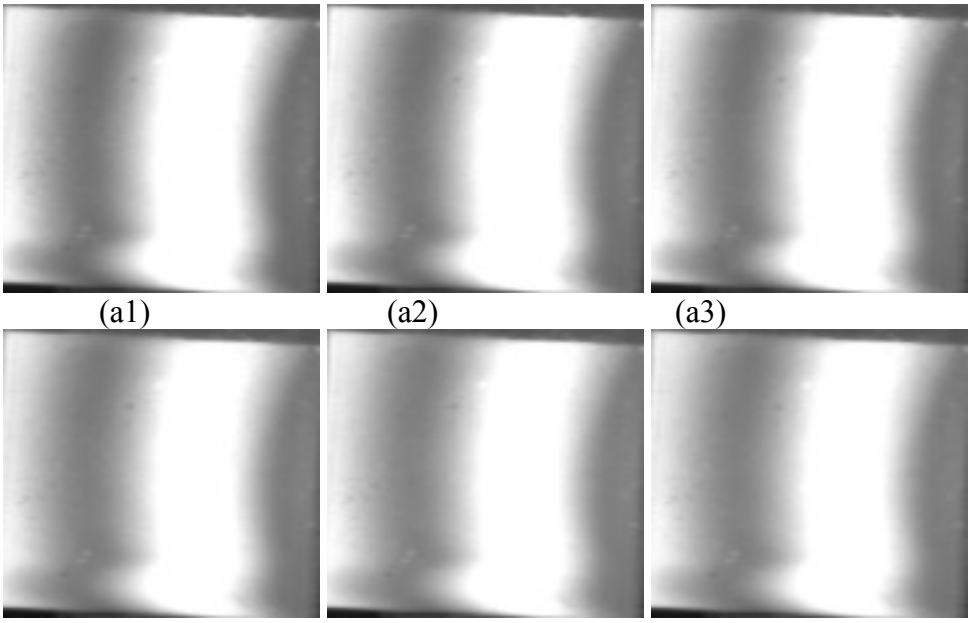

(a1) (a2) (a3)

(b1) (b2) (b3)

Figure 3.6: Image pairs (a) Fringes for α=40°, β=0°, θ=50°, g= 0.2mm at starting position. (b) Fringes after contour interval of (1) 0.365, (2) 0.367, (3) 0.369(mm)

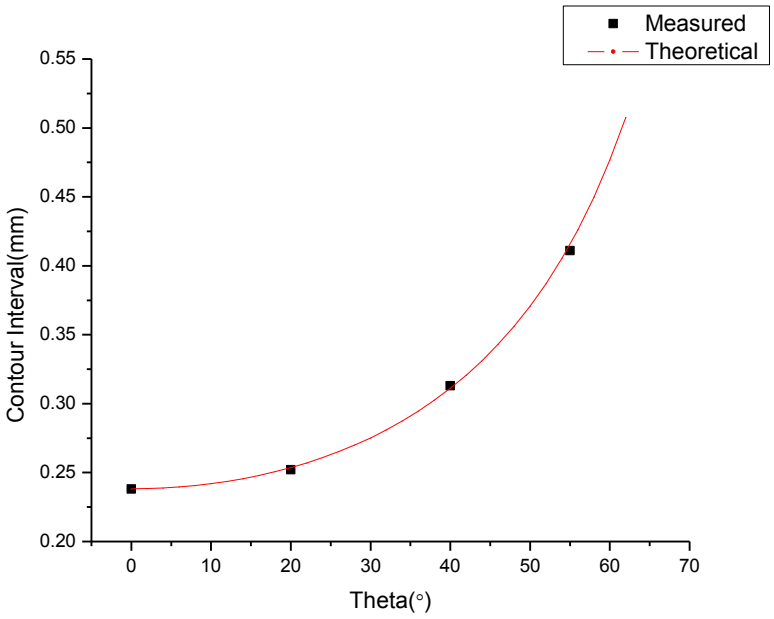

Figure 3.7: Experimental data compared with theoretical values for setup of α = 40°, β = 0° and g= 0.2mm

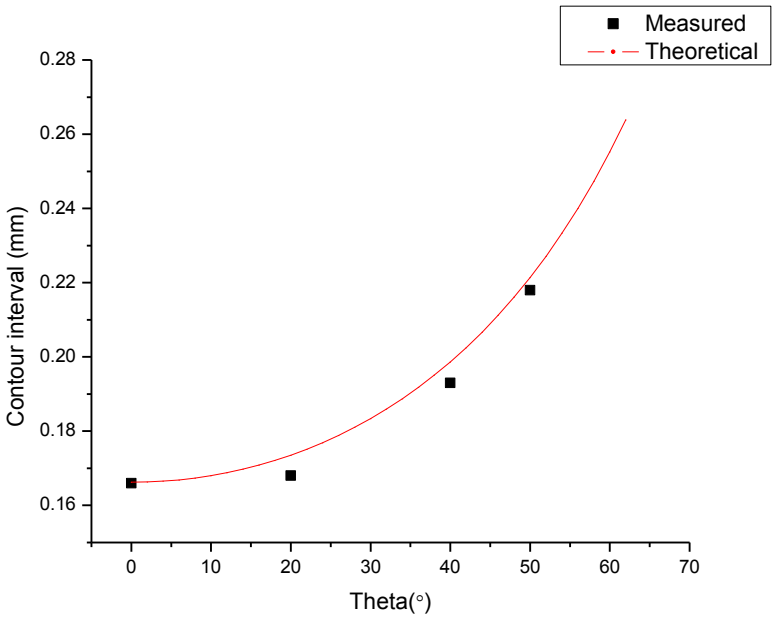

Figure 3.8: Experimental data compared with theoretical values for setup of α = 40°, β = 20° and g= 0.2mm.

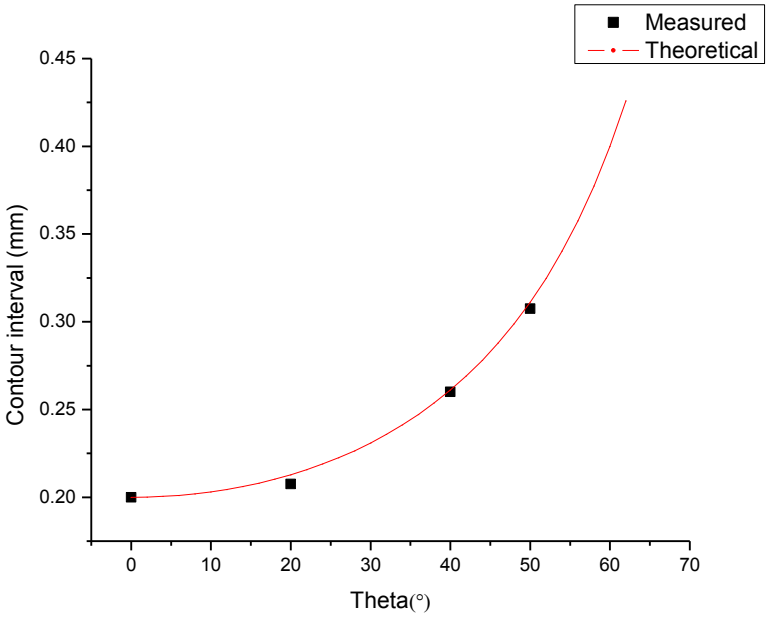

Figure 3.9: Experimental data compared with theoretical values for setup of α = 45°, β = 0° and g= 0.2mm

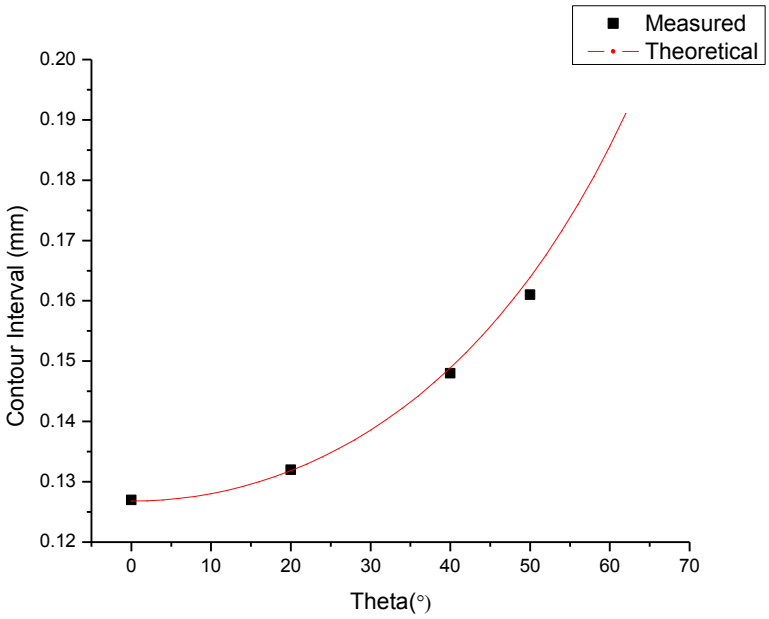

Figure 3.10: Experimental data compared with theoretical values for setup of α = 40°, β = 30° and g=0.2mm

Application of Advanced Technique

The technique was tested on a processor package to demonstrate the increase of sensitivity with the use of non-normal angles. The specimen tested was a 35mmx35mm plastic ball grid array (PBGA) package from Marvell. The package was prepared with white paint on the side with the ball grid array.

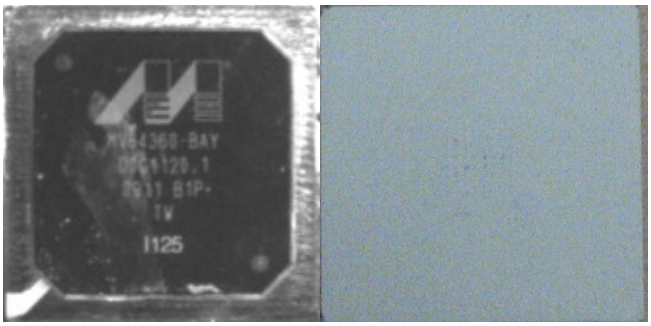

Figure 3.11: Marvell PBGA Package (left) front (right) back

The α angle was kept constant at 63° to maintain both high sensitivity and high contrast. The specimen was placed within the zero-Talbot distance in order to maximize contrast. The package was examined under three conditions: normal incidence, non-normal incidence, and non-normal incidence with non-coplanar light. The setup configuration was the same as the verification experiment. Images were taken at one-quarter of the contour interval to approximate phase changes of 90°. The four images were then used with the Moiré program to determine the displacement. The contour intervals achieved were 0.1mm for normal incidence, 0.082mm for a β=25°, and a contour interval of 0.0542 for the non-coplanar setup.

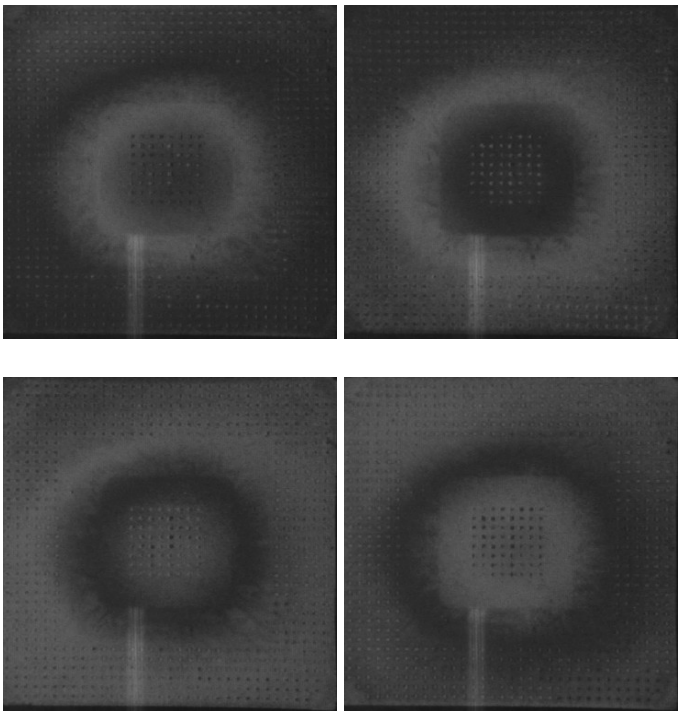

(a)

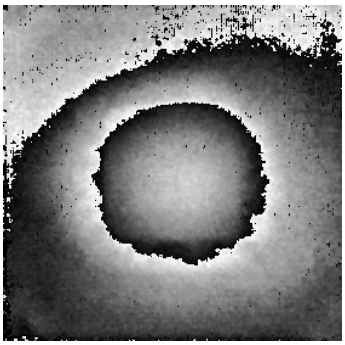

(b)

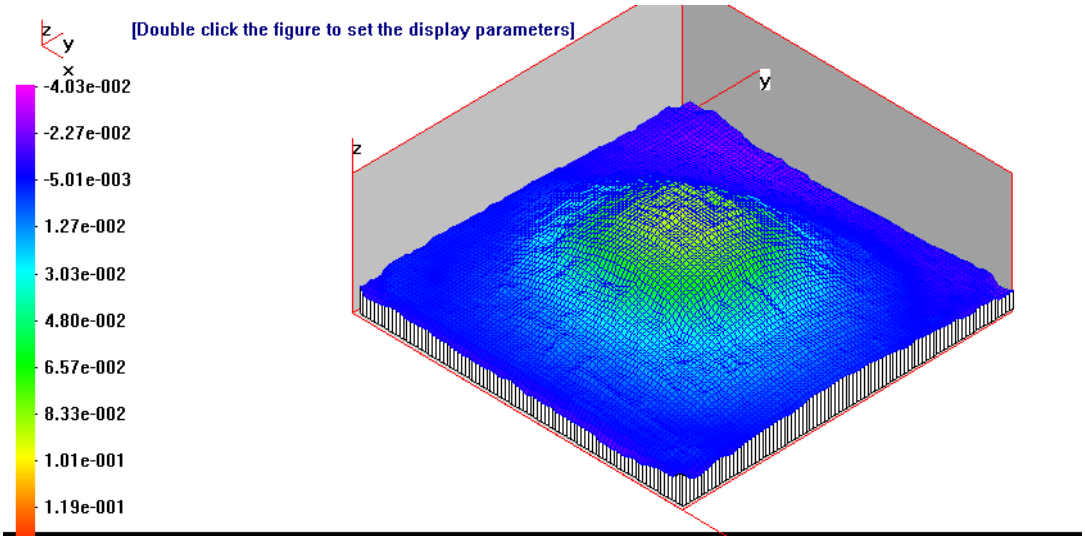

(c)

Figure 3.12: Setup of α=63°, β=0°, θ=0°, g=0.2mm a) Phase shifted images of specimen b) Specimen wrapped phase map c) 3D-model of displacement pattern

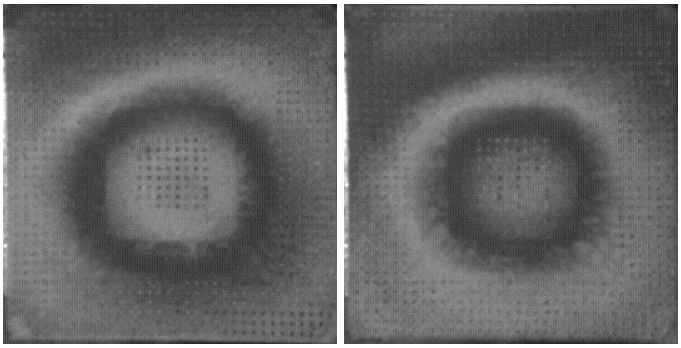

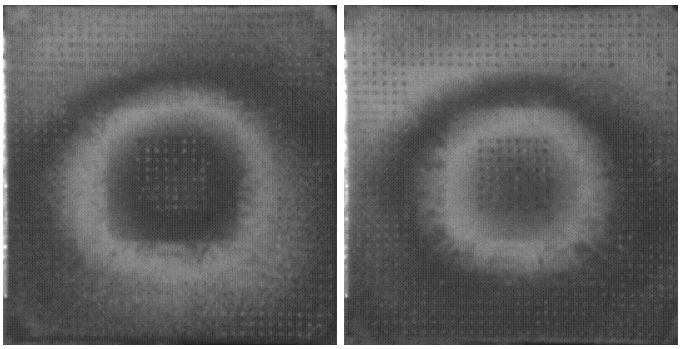

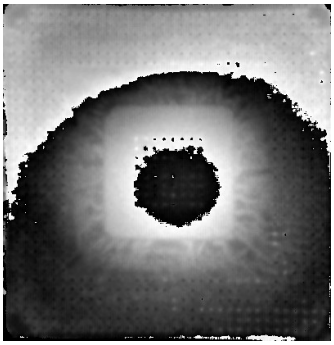

(a) (b)

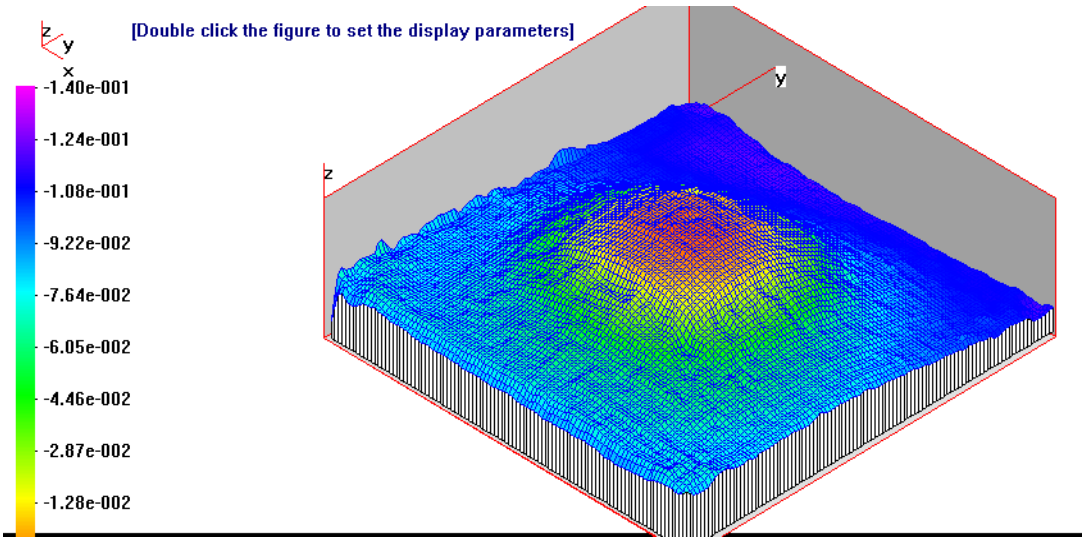

(c)

Figure 3.13: Setup of α=63°, β=25°, θ=0°, g=0.2mm a) Phase shifted images of specimen b) Specimen wrapped phase map c) 3D-model of displacement pattern

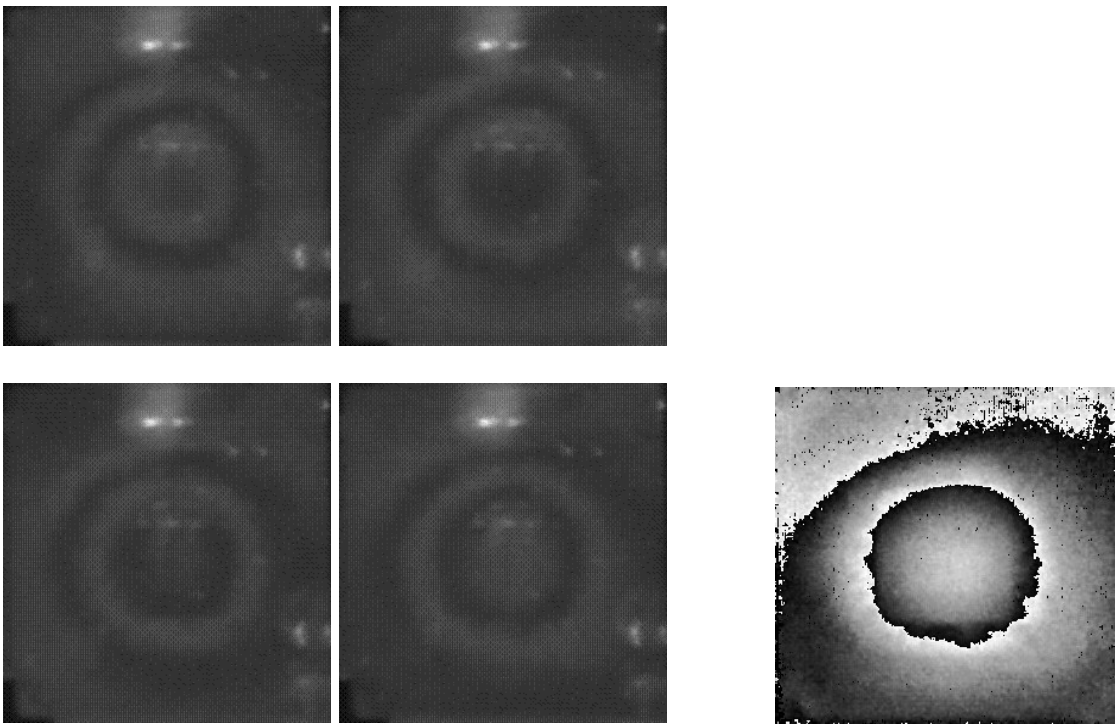

(a) (b)

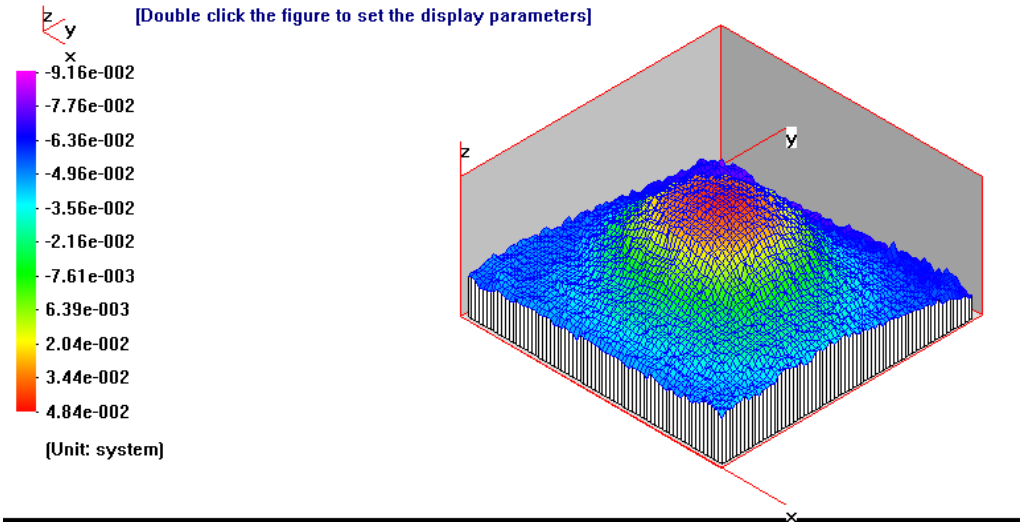

(b)

Figure 3.14: Setup of α=63°, β=60°, θ=20°, g=0.2mm a) Phase shifted images of specimen b) Specimen wrapped phase map c) 3D-model of displacement pattern

The relative displacement in all the forward stated conditions was in agreement with each other showing that the setups are consistent. The peak relative displacement value was 0.1mm. The increase in the number of fringes is readily seen between the normal configuration, as shown in Figure 3.12, and the new modified technique as shown in Figure 3.14. As expected, the new configuration has doubled the number of visible fringes, since the large β gives a contour interval of $\frac{g}{\tan\alpha = 63° + \tan\beta = 60°} = \frac{g}{3.69}$ in comparison to the normal configuration which gives an interval of $\frac{g}{\tan\alpha = 63° + \tan\beta = 0°} = \frac{g}{2}$. The increase in sensitivity can be seen in the better definition of the warpage seen in Figure 3.14c. The influence of small β angles can be seen, as only one fringe appears in Figure 3.13a, which is the same number of fringes seen in the normal configuration of Figure 3.12a. The gain of a single fringe becomes important when measurements are needed with partial fringes in the normal viewing configuration.

Chapter 4: Potential Future Investigation

One of the applications of shadow moiré is high-temperature warpage measurements. In existing tests [21], a convection oven is used, where there is typically slits for light to enter and exit. A new system setup without the constraint imposed by the oven is necessary for a dynamically configurable shadow moiré system. To achieve this, a conduction heater could be used as the heating source to replace the oven. The rest of the setup could then be fitted accordingly with the grating being the moving part. This would also potentially eliminate warpage of the reference grating from the heating.

The shadow moiré implementation depends on the accurate positioning of both the illuminator source and the camera. A major issue with the use of non-normal angles is that the distance between the light source and the camera could get prohibitively large in order to obtain the correct angles. A modification to the technique would be to use collimating lens, as shown in the second setup in Figure 2.3. This setup is not distance based, versus the current setup which requires the camera and light to be placed apart from each other at four times the distance from the sample to the height of the camera/light source. However, this change would be application specific as the sample size that can be measured is dependent on the collimating lens, whereas no such limitation is present in the current technique. .

Chapter 5: Conclusions

The need for better sensitivity warpage measurements comes from the electronics industry's smaller package profile. The use of non-normal angles was utilized to increase the base sensitivity. However, with a range of angles not accessible in a traditional setup, a modification to the configuration was implemented. A new governing equation was derived and experimentally verified over different α and β angles. This showed that large rotations could potentially nullify the benefits of non-normal angles. However, at the smaller rotation angles, even up to 30°, the difference in contour interval from the normal viewing is very small. Therefore, a new range of angles could now be utilized. The warpage of a processor package was then measured to demonstrate the increase in sensitivity gained by using the non-normal angles. This experiment showed that the contour interval could be reduced by almost in half as compared to normal viewing. The new configuration was shown to be application dependent, with improvements to sensitivity and dynamic range limitations driving its implementation.

Bibliography

[1] I. T. R. f. Semiconductors. (2009). Assembly and Packaging 2009 Edition.

[2] R. Tammula, E. Rymaszewski, and A. Klopfenstein, eds., “Microelectronics Packaging Handbook,” Kluwer Academic, Norwell (1997).

[3] A. Cox, "Development of Advanced Shadow Warpage Measurement Systems: Shadow Moiré with Nonzero Talbot Distance and Far Infrared Twyman-Green Interferometry," M.S., Mechanical Engineering, University of Maryland, College Park, 2006.

[4] H. Takasaki, "Moiré Topography," Appl. Opt., vol. 9, pp. 1467-1472, 1970.

[5] D. M. Meadows, W. O. Johnson, and J. B. Allen, "Generation of Surface Contours by Moiré Patterns," Appl. Opt., vol. 9, pp. 942-947, 1970.

[6] J. S. S. T. Association, "High Temperature Package Warpage Measurement Methodology," vol. JESD22-B11, ed, 2005.

[7] J. A. Gómez-Pedrero, J. A. Quiroga, M. José Terrón-López, and D. Crespo, "Measurement of surface topography by RGB Shadow-Moiré with direct phase demodulation," Optics and Lasers in Engineering, vol. 44, pp. 1297-1310, 2006.

[8] K. C. Yuk, J. H. Jo, and S. Chang, "Determination of the absolute order of shadow moiré fringes by using two differently colored light sources," Appl. Opt., vol. 33, pp. 130-132, 1994.

[9] S. Song, F. Zhu, W. Zhang, and S. Liu, "Warpage measurement of various substrates based on white light shadow moire technology," pp. 389-392, 2011.

[10] M. Amagai and Y. Suzuki, "A study of package warpage for package on package (PoP)," in Electronic Components and Technology Conference (ECTC), 2010 Proceedings 60th, 2010, pp. 226-233.

[11] T. Ming-Yi, C. Hsing-Yu, and M. Pecht, "Warpage Analysis of Flip-Chip PBGA Packages Subject to Thermal Loading," IEEE Transactions on Device and Materials Reliability, vol. 9, pp. 419-424, 2009.

[12] Y. Chao-Pin, C. Ume, R. E. Fulton, K. W. Wyatt, and J. W. Stafford, "Correlation of analytical and experimental approaches to determine thermally induced PWB warpage," Components, Hybrids, and Manufacturing Technology, IEEE Transactions on, vol. 16, pp. 986-995, 1993.

[13] T. C. Chiu, H. W. Huang, and Y. S. Lai, "Warpage evolution of overmolded ball grid array package during post-mold curing thermal process," Microelectronics Reliability, vol. 51, pp. 2263-2273, Dec 2011.

[14] D. Hai, R. E. Powell, C. R. Hanna, and I. C. Ume, "Warpage measurement comparison using shadow moire and projection moire methods," Components and Packaging Technologies, IEEE Transactions on, vol. 25, pp. 714-721, 2002.

[15] D. Hai, I. C. Ume, R. E. Powell, and C. R. Hanna, "Parametric study of warpage in printed wiring board assemblies," Components and Packaging Technologies, IEEE Transactions on, vol. 28, pp. 517-524, 2005.

[16] T. Ming-Yi, Y. C. Chen, and S. W. R. Lee, "Correlation Between Measurement and Simulation of Thermal Warpage in PBGA With

Consideration of Molding Compound Residual Strain," Components and Packaging Technologies, IEEE Transactions on, vol. 31, pp. 683-690, 2008.

[17] Y. Polsky, W. Sutherlin, and I. C. Ume, "A comparison of PWB warpage due to simulated infrared and wave soldering processes," Electronics Packaging Manufacturing, IEEE Transactions on, vol. 23, pp. 191-199, 2000.

[18] M. Y. Tsai, C. W. Ting, C. Y. Huang, and Y. S. Lai, "Determination of residual strains of the EMC in PBGA during manufacturing and IR solder reflow processes," Microelectronics Reliability, vol. 51, pp. 642-648, Mar 2011.

[19] S. Y. Yang, Y.-D. Jeon, S.-B. Lee, and K.-W. Paik, "Solder reflow process induced residual warpage measurement and its influence on reliability of flip-chip electronic packages," Microelectronics Reliability, vol. 46, pp. 512-522, 2006.

[20] C. P. Yeh, K. Banerjee, T. Martin, C. Ume, R. Fulton, J. Stafford, and K. Wyatt, "Experimental and analytical investigation of thermally induced warpage for printed wiring boards," in Electronic Components and Technology Conference, 1991. Proceedings., 41st, 1991, pp. 382-387.

[21] K. Verma, D. Columbus, and B. Han, "Development of real time/variable sensitivity warpage measurement technique and its application to plastic ball grid array package," Electronics Packaging Manufacturing, IEEE Transactions on, vol. 22, pp. 63-70, 1999.

[22] Y. Y. Wang and P. Hassell, "Measurement of thermally induced warpage of BGA packages/substrates using phase-stepping shadow moire," in Electronic

Packaging Technology Conference, 1997. Proceedings of the 1997 1st, 1997, pp. 283-289.

[23] C. Han, "Shadow Moiré Using Non-Zero Talbot Distance and Application of Diffraction Theory to Moiré Interferometry," PHD, Mechanical Engineering, University of Maryland College Park, 2005.

[24] C. W. Han and B. Han, "High Sensitivity Shadow Moiré Using Nonzero-Order Talbot Distance," Experimental Mechanics, vol. 46, pp. 543-554, 2006.

[25] T. Yoshizawa and T. Tomisawa, "Shadow Moire Topography by Means of the Phase-Shift Method," Optical Engineering, vol. 32, pp. 1668-1674, Jul 1993.

[26] Z. Wang, "Development and Application of Computer Aided Fringe Analysis," PHD, University of Maryland, College Park, 2003.

[27] T. Hoang, Z. Y. Wang, M. Vo, J. Ma, L. Luu, and B. Pan, "Phase extraction from optical interferograms in presence of intensity nonlinearity and arbitrary phase shifts," Applied Physics Letters, vol. 99, Jul 18 2011.

[28] H. Du, H. Zhao, B. Li, Z. Li, L. Zheng, and L. Feng, "Algorithm for phase shifting shadow moiré with an unknown relative step," Journal of Optics, vol. 13, p. 035405, 2011.

[29] C. Kuo-Shen, T. Y. F. Chen, C. Chia-Cheng, and I. K. Lin, "Full-field wafer level thin film stress measurement by phase-stepping shadow Moire," Components and Packaging Technologies, IEEE Transactions on, vol. 27, pp. 594-601, 2004.

[30] J. Liao and A. Voloshin, "Enhancement of the shadow-moiré method through digital image processing," Experimental Mechanics, vol. 33, pp. 59-63, 1993.

[31] E. Hack and J. Burke, " Measurement uncertainty of linear phase-stepping algorithms," Review of Scientific Instruments, vol. 82, p. 061101, 2011.

[32] C. Han and B. Han, "Error Analysis of Phase Shifting Technique When Applied to Shadow Moiré," Applied Optics, vol. 45, p. 1124, 2006.

[33] Y. Arai and S. Yokozeki, "Improvement of measurement accuracy in shadow moire by considering the influence of harmonics in the moire profile," Appl Opt, vol. 38, pp. 3503-7, Jun 1 1999.

[34] J. C. Martinez-Anton, H. Canabal, J. A. Quiroga, E. Bernabeu, M. A. Labajo, and V. C. Testillano, "Enhancement of surface inspection by Moiré interferometry using flexible reference gratings," Opt. Express, vol. 8, pp. 649-654, 2001.

[35] A. M. F. Wegdam, O. Podzimek, and H. T. Bösing, "Simulation of shadow moiré systems containing a curved grating surface," Appl. Opt., vol. 31, pp. 5952-5955, 1992.

[36] Daniel Post, B. Han, and P. Ifju, High Sensitivity Moire: Experimental Analysis for Mechanics and Materials New York: Springer-Verlag 1994.

[37] C. W. Ackerman, "Development of a Real-time High Sensitivity Shadow Moire System and its Application to Microelectronics Packaging," M.S., Mechanical Engineering, Clemson University, 2000

[38] M. Testorf, "Talbot Effect for Oblique Angle of Light Propagation," Optics Communications, vol. 129, pp. 167-172, Aug 15 1996..

[39] C. Han and B. Han, "Contrast of shadow moiré at high-order Talbot distances," Optical Engineering, vol. 44, p. 028002, 2005.

[40] S. Wei, S. Wu, I. Kao, and F. P. Chiang, "Measurement of Wafer Surface Using Shadow Moire Technique With Talbot Effect," Journal of Electronic Packaging, vol. 120, pp. 166-170, 1998.

[41] O. Kafri and E. Keren, "Fringe observation and depth of field in moire analysis," Appl Opt, vol. 20, pp. 2885-6, Sep 1 1981.